

Gapless spin liquid state of the spin- $\frac{1}{2}$ honeycomb antiferromagnetic Γ model

Qiang Luo,^{1,2} Jize Zhao,^{3,*} Hae-Young Kee,^{2,4} and Xiaoqun Wang^{5,6,†}

¹Department of Physics, Renmin University of China, Beijing 100872, China

²Department of Physics, University of Toronto, Toronto, Ontario M5S 1A7, Canada

³School of Physical Science and Technology & Key Laboratory for Magnetism and Magnetic Materials of the MoE, Lanzhou University, Lanzhou 730000, China

⁴Canadian Institute for Advanced Research, Toronto, Ontario, M5G 1Z8, Canada

⁵Key Laboratory of Artificial Structures and Quantum Control (Ministry of Education), School of Physics and Astronomy, Tsung-Dao Lee Institute, Shanghai Jiao Tong University, Shanghai 200240, China

⁶Beijing Computational Science Research Center, Beijing 100084, China

(Dated: June 7, 2022)

To understand the ground state of the spin-1/2 honeycomb Γ antiferromagnet (HCTA), we propose a choreographed model which includes a bond-modulated Heisenberg interaction (J) aside from the Γ term. By varying $\vartheta = \text{atan}(\Gamma/J)$ in $[0, \pi]$, we demonstrate that the classical ground state changes from a zigzag order to a stripy order, through an extensive intermediate region. Using the linear spin-wave theory we find that the sublattice magnetization of the zigzag order is dramatically suppressed when close to HCTA. The intermediate region is fragile against quantum fluctuations and gives way to a gapless quantum spin liquid (QSL) phase in a wide interval of $0.50 \lesssim \vartheta/\pi \leq 0.66(1)$ at the quantum level. Based on a series of compelling evidences including the vanishing magnetic and nematic orders, and also a perceptible correlation of the hexagonal plaquette operator, we conclude that the ground state of HCTA is a gapless QSL phase with a plaquette correlation.

Introduction. – The ongoing search for exotic magnetic states in highly frustrated antiferromagnets [1–4] has been extended to a new class of correlated materials with a two-dimensional (2D) honeycomb structure[5–7] and its three-dimensional variants[8]. It is suggested[9] that bond-dependent interactions[10] could be realized in the spin-orbit coupled Mott insulators with the aforementioned lattice geometry. In particular, the Kitaev interaction is one of the most outstanding examples and its ground state is the Kitaev quantum spin liquid (QSL) which hosts fractionalized Majorana fermions and flux excitations[11]. Realization of the Kitaev interaction in real materials was first proposed in iridates [12–14], and then turned toward α -RuCl₃ in which Ru³⁺ ions are arranged in a honeycomb lattice and carry effective spin-1/2 particles [5–7, 15]. Although α -RuCl₃ displays long-range zigzag magnetic order at low temperature [16–22], it is argued to be proximate to the Kitaev QSL owing to the broad continuum of magnetic excitations identified in Raman scattering[23, 24] and inelastic neutron scattering[6, 7, 25–27].

Even though considerable attention has been attracted by the Kitaev interaction [28–40], it is evidential that a sizable antiferromagnetic (AFM) off-diagonal symmetric Γ interaction is also of vital importance to α -RuCl₃ and other materials (see refs. [41–43] and references therein) and thus should be considered on an equal footing[44–50]. Crucially, it is shown that the Γ interaction may be responsible for the strongly anisotropic responses to the magnetic field observed in α -RuCl₃[41, 51]. In contrast to the Kitaev honeycomb model[11], analytical solution of the honeycomb Γ antiferromagnet (HCTA) has not been found yet[52]. Given its infinite classical ground-state

degeneracy[53], determining the precise quantum nature of HCTA is nontrivial, and existing numerical works have already led to conflicting results. Parallel works by exact diagonalization of small cluster[54] and density-matrix renormalization group (DMRG) study of narrow infinite cylinder[55] both claim that the ground state is a non-magnetic phase. Recent variational Monte Carlo simulation, however, suggests that it is preferably a zigzag order[56].

In this letter, we employ the 2D DMRG method[57, 58] to explore the nature of the spin-1/2 HCTA. We propose a model which consists not only of the Γ term, but also of a bond-modulated Heisenberg interaction, dubbed the bond-modulated J - Γ (BMJ Γ) model. We emphasize that this model is not a description of any particular material. Instead, it works as a virtuous arena to clarify the debates by unfolding the competing states. Apart from a zigzag order, our model surprisingly harbors a gapless QSL with a plaquette correlation. The ground state of HCTA continuously connected to this QSL and is separated from the zigzag order by first-order transition.

Model. – The Hamiltonian of the BMJ Γ model reads

$$\mathcal{H} = J \sum_{\langle ij \rangle} \eta_{ij} \mathbf{S}_i \cdot \mathbf{S}_j + \Gamma \sum_{\langle ij \rangle \parallel \gamma} (S_i^\alpha S_j^\beta + S_i^\beta S_j^\alpha) \quad (1)$$

where S_i^γ ($\gamma = x, y,$ and z) is the γ -component of a spin-1/2 operator at site i , and α and β are the two other bonds on a honeycomb lattice. $\eta_{ij} = 1$ for the bond $\langle ij \rangle$ along the horizontal direction and equals to -1 otherwise (see Fig. 1(a)). Throughout the following, J and Γ are parameterized using $\vartheta \in [0, \pi]$ so as to $J = \cos \vartheta$ and $\Gamma = \sin \vartheta$ (≥ 0). The large-scale 2D DMRG calculations are performed mainly on two kinds of cluster geometries.

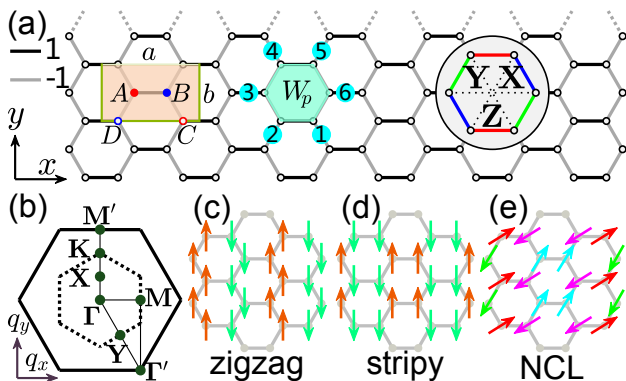


FIG. 1: (a) Illustration of an XC6 cylinder on a honeycomb lattice. η_{ij} is +1 (−1) for horizontal (zigzag) bonds. The insets are (left) the unit cell for the zigzag/stripy order, (middle) the hexagonal plaquette operator W_p with its six sites enumerated, and (right) the **X** (blue), **Y** (green), and **Z** (red) bonds. (b) First and second Brillouin zones of a honeycomb lattice. (c) and (d) depict the zigzag order and stripy order, respectively. (e) A noncollinear phase with a unit cell of 4×2 .

One is a $L_x \times L_y$ XC n cluster under cylindrical boundary condition[59, 60]. We consider even circumferences n ($= L_y/a_0$) ranging from 4 to 10 lattice spacing a_0 , and use fixed ratio $L_x/L_y = 2$ unless stated explicitly otherwise. $N = L_x L_y$ is the total number of spins. The other is a C_6 symmetric hexagonal cluster with $N = 24$ or 32 sites under full periodic boundary conditions (see the Supplemental Material (SM) for detail[61]). In both cases, we keep up to $m = 3000 \sim 5000$ states and perform about 12 sweeps so as to ensure the truncation error is smaller than 10^{-6} .

Classical phase diagram. – Intuitively, the classical ground states of Eq. (1) with ϑ/π equaling to 0 and 1, are zigzag order (see Fig. 1(c)) and stripy order (see Fig. 1(d)), respectively. Due to the bond-modulated η_γ -factor, the other two zigzag orders with different spin orientations are not equivalent to the one shown in Fig. 1(c), and are called as twining zigzag orders[61]. For general ϑ , spin configurations are determined by the parallel tempering Monte Carlo (PTMC) simulation[67, 68] in which the spins \mathbf{S}_i are treated as $O(3)$ vectors with the magnitude $|\mathbf{S}_i| = S$. The computations are performed on XC clusters and the ground-state energy $e_g = E_g/(NS^2)$ (E_g is the total energy) is shown in Fig. 2(a). The left side is the zigzag order with $e_g^{zz} = -(2\Gamma + 3J)/2$ and its magnetic moment direction is parallel to $\mathbf{n} [11\bar{1}]$. The majority of the right side is occupied by the stripy order with $e_g^{st} = -(\Gamma - 3J)/2$. As shown in the SM[61], there is an emergent continuous symmetry for the stripy order. Further, an extensive intermediate region appears in between. It is dominated by a so-called mixed phase in which the AFM order and two twining zigzag orders are degenerate with energy $e_g^{\text{mixed}} = -(2\Gamma - J)/2$ [61]. The zigzag-mixed transition takes place exactly at $\vartheta_{t,l}^{\text{cl}}/\pi =$

0.5. As a contrast, there is no direct transition between the mixed phase and the stripy phase expected to occur at $\vartheta_{t,r}^{\text{cl}}/\pi = 1 - \frac{1}{\pi} \text{atan} 2 \approx 0.6476$. Instead, an unforeseen noncollinear (NCL) phase with $e_g^{\text{NCL}} = -\sqrt{J^2 + \Gamma^2/16} - \Gamma/\sqrt{2}$ appears in a rather narrow region (the window of ϑ/π is less than 0.02, see inset of Fig. 2).

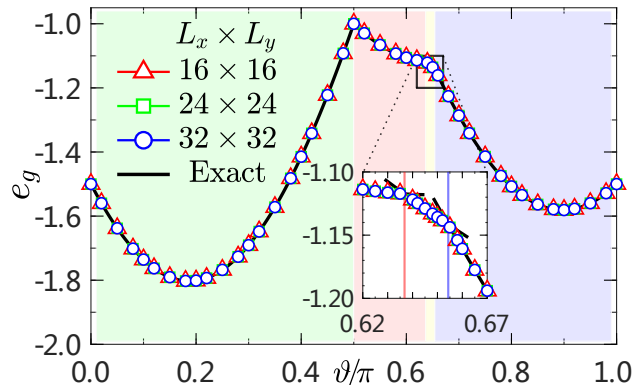


FIG. 2: Classical ground-state energy e_g obtained by PTMC simulations. The solid black line represents the exact solution. Inset: Zoom in of the energy curves near $\vartheta_{t,r}^{\text{cl}}/\pi$.

Spin-wave theory. – Proceeding with a standard linear spin-wave theory (LSWT) analysis via Holstein-Primakoff transformation[69], we obtain the following Hamiltonian: $\mathcal{H} = E_g[S^2 \rightarrow S(S+1)] + \frac{J}{2} \sum_{\mathbf{q}} \psi_{\mathbf{q}}^\dagger \mathcal{M}_{\mathbf{q}} \psi_{\mathbf{q}}$, where $\psi_{\mathbf{q}}^\dagger = (a_{\mathbf{q}}^\dagger, b_{\mathbf{q}}^\dagger, \dots, a_{-\mathbf{q}}, b_{-\mathbf{q}}, \dots)$ is the Nambu spinor, and $\mathcal{M}_{\mathbf{q}}$ is a 2×2 block matrix whose explicit forms are shown in the SM[61]. The four spin-wave dispersion branches $\omega_{\mathbf{q}\nu}$ ($\nu = 1-4$) for the zigzag order ($\vartheta/\pi=0.25$) and stripy order ($\vartheta/\pi=0.75$) are shown in Fig. 6 of the SM. The spectra are symmetric with the middle of the Γ - \mathbf{M} line, so the Γ and \mathbf{M} points are equivalent. There exist a magnon gap Δ at \mathbf{M} point for the zigzag order. When approaching HCGA, $J/\Gamma \ll 1$, the gap vanishes as $\Delta/\Gamma \simeq \frac{\sqrt{30}}{3} \sqrt{J/\Gamma}$. Due to the emergent continuous symmetry of the stripy order, the magnon spectra are gapless. However, as shown in Fig. 5 of the SM[61], those macroscopic degeneracy would be lifted via an order-by-disorder mechanism[70], selecting only two of them that break lattice rotational symmetry.

Gapless QSL phase. – In the two limits with $\vartheta/\pi = 0$ and 1, quantum fluctuations are too weak to alter the underlying zigzag order[71] and stripy order[72]. Although whether there is a direct transition or an intervening zone that impedes the direct transition is unclear *a priori*, the sublattice magnetization by LSWT can be helpful to shed light on the nature of transitions. It is found that the magnetization $\langle M \rangle$ of the zigzag order has a suppression dramatically and vanishes at $\vartheta_{t,l}^{\text{cl}}/\pi = 0.50$ [61]. The magnetization of the stripy order near $\vartheta_{t,r}^{\text{cl}}/\pi \approx 0.6476$ is not totally dismissed but only has a half shrinkage[61].

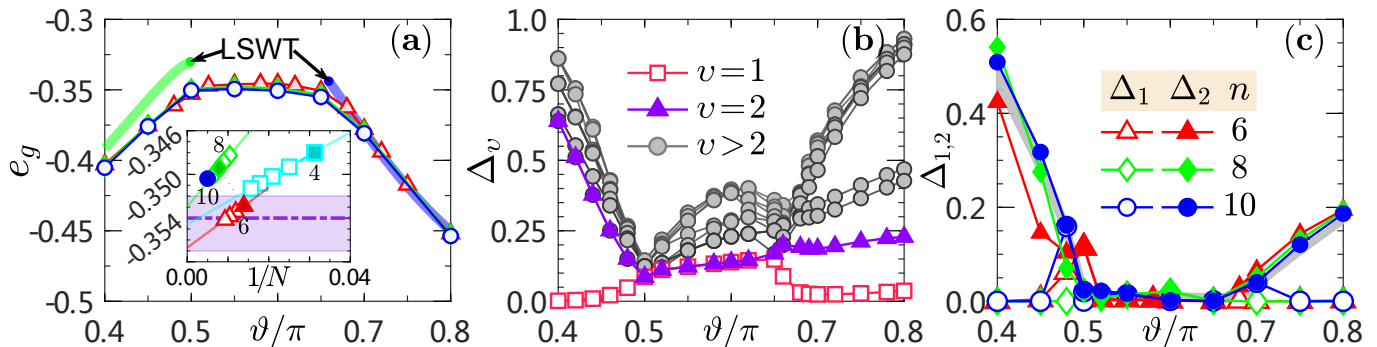


FIG. 3: (a) Quantum ground-state energy e_g under three XC clusters where the circumferences n are 6 (red triangle), 8 (green diamond), and 10 (blue circle). The thick belts are the LSWT energy. Inset: Extrapolation of energy for HCTA. For each circumferences n the energy is linearly decreasing with $1/N$ and the special cases ($L_x/L_y = 2$) are marked by filled symbols. The extrapolated values fall in the band centered at $-0.354(3)$ [61]. (b) The first fifteen excitation gaps Δ_v with degeneracy for a $N = 24$ hexagonal cluster. (c) The two lowest excitation gaps Δ_1 (open symbols) and Δ_2 (filled symbols) at three XC clusters; The thick belt is the extrapolated bulk gap.

Besides, the spin-wave energy reduction δE of the zigzag order is more pronounced than that of the stripy order, suggesting the strong quantum fluctuations near HCTA. The spin-wave energy in the mixed phase, say Néel order, is overwhelmingly higher than its neighbors[61], making the authentic phase somewhat unpredictable.

To clarify this issue, we show the DMRG results of the ground-state energy $e_g = E_g/N$ on three XC clusters in Fig. 3(a). The energy curves in the middle are very flat, while they have two sharp downwarping when away from it, leading to two well-marked kinks that are signals of first-order transitions. The energy e_g at $\vartheta/\pi = 0.5$ exhibits a nonmonotonic fall with the increasing of circumference n . Extrapolation of the energy in the thermodynamic limit (TDL) is intractable, and an elaborate analysis suggests that $e_g = -0.354(3)$ (see Fig. 8 of the SM[61]). Fig. 3(b) shows the first fifteen low-lying excitation gaps, $\Delta_v = E_v - E_g$, on a $N = 24$ hexagonal cluster. It can be seen that Δ_1 vanishes while Δ_2 survives in the zigzag/stripy phases, indicating double degenerate ground states. For the intermediate region, the ground state is unique and the level spacing is denser than its neighbors. Such a collapse of excitation gaps could be interpreted as a sign of gapless spectra[32]. We also present the two lowest excitation gaps on three large XC clusters. The excitation gap in the middle is extremely small as compared to the $N = 24$ case, indicating that it closes rapidly with the size increased. As shown in the SM[61], the excitation gap at $\vartheta/\pi = 0.50$ is also terminated within a sustainable round-off. Taken together, we draw the conclusion that there is a gapless intermediate phase when $\vartheta_{t,l} \leq \vartheta \leq \vartheta_{t,r}$ with $\vartheta_{t,l}/\pi \simeq 0.50$ and $\vartheta_{t,r}/\pi = 0.66(1)$.

To advocate the gapless nature of HCTA, we calculate the excitation gap on cylinders of $2 \times L_x \times L_y$ (see inset of Fig. 4) with $N = 2L_xL_y$ sites in total. Although the three-leg cylinder is gapped, excitation gap

for cylinder of $L_y = 4$ decreases with L_x and promise to vanish as $L_x \rightarrow \infty$ [73]. In this circumstance, we calculate the von Neumann entanglement entropy \mathcal{S} and perform the entanglement entropy scaling according to $\mathcal{S} = \frac{c}{6} \ln(\frac{2L_x}{\pi}) + c'$ where c is the central charge[74]. Figure 4 shows that \mathcal{S} obeys this formula well and gives a central charge which is close to 1. Furthermore, we also find that \mathcal{S} approximately goes with the circumference up to a logarithmic correction under the similar cylinders of $L_x/L_y = 2$ [61], consistent with the critical behavior of HCTA.

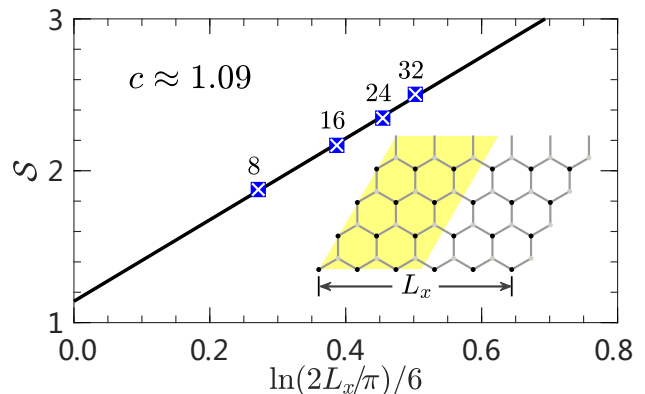


FIG. 4: Entanglement entropy on $L_y = 4$ cylinders of length L_x . The inset shows the bipartite partition of a cylinder.

The magnetic order parameter is defined by $M_N(\mathbf{Q}) = \sqrt{\mathbb{S}_N(\mathbf{Q})/N}$ where $\mathbb{S}_N(\mathbf{Q})$ is the static magnetic structure factor with \mathbf{Q} being the ordering wavevector[75]. As seen from Fig. 5(a), order parameters of the zigzag and stripy phases exhibit maxima at $\vartheta/\pi \approx 0.25$ and 0.75 , respectively. The magnetic order in the intermediate region is dramatically suppressed, followed by an algebraically decay with the circumference n (see Fig. 5(b) and Fig. 5(c)). After a careful inspection of the finite-

size effect, we infer that it will disappear eventually. Specifically, our best fitting gives $M \simeq 0.0000(2)$ for HCGA ($\vartheta/\pi = 0.5$). We also resort to a complementary strategy by applying pinning fields on a finite long cylinder, and the vanishing pinning order in the middle is fairly consistent with an intervening QSL phase[61].

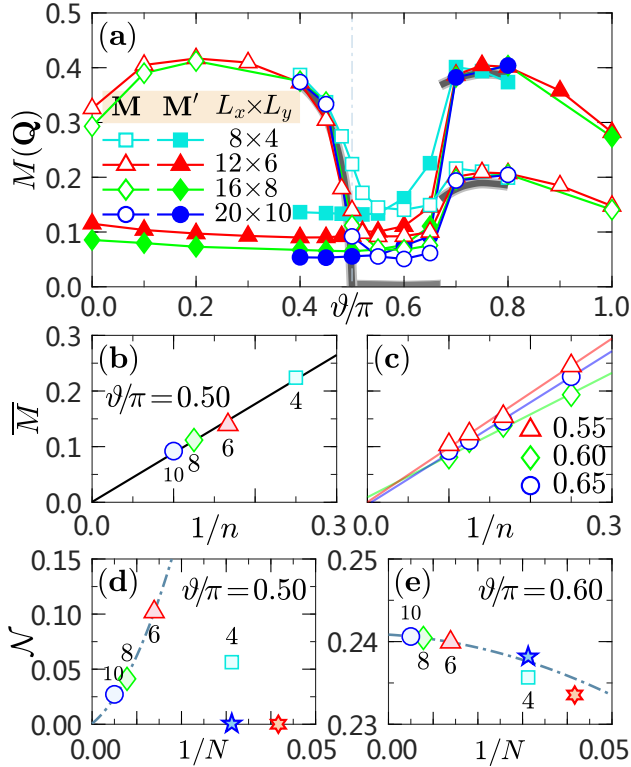


FIG. 5: (a) Order parameters $M(\mathbf{Q})$ for the zigzag order (open symbols) and stripy order (filled symbols) with $\mathbf{Q} = \mathbf{M}$ and/or \mathbf{M}' under four finite XC clusters. The thick gray line shows the magnetic order in TDL. Extrapolations of the maximal peaks \bar{M} are shown in (b) $\vartheta/\pi = 0.50$ and (c) $\vartheta/\pi = 0.55$ (red triangle), 0.60 (green diamond), and 0.65 (blue circle). (d) and (e) shows the finite-size scaling of the Lattice nematic order \mathcal{N} at $\vartheta/\pi = 0.50$ and $\vartheta/\pi = 0.60$, respectively. Nematic orders under hexagonal clusters of $N = 24$ (red hexagram) and 32 (blue pentagram) are also shown for reference.

We turn to the lattice nematicity by measuring the bond energies E_γ ($\gamma = x, y, \text{ and } z$). Motivated by the bond-modulated η_γ -factor in model Eq. (1), we introduce a lattice nematic order parameter $\mathcal{N} = E_{x/y} - E_z$ [76, 77]. As illustrated in Fig. 5(d), the nematic order at $\vartheta/\pi = 0.50$ is speculated to vanish in the TDL since it is infinitesimally small for clusters of $N = 24$ and 32 . In addition, although there are nonzero values at finite XC clusters, a quadratic fit of the largest three sizes suggests that the nematic order vanishes ultimately, showing that there is no spontaneous breaking of C_6 rotational symmetry. However, there is a trivial nematicity at $\vartheta/\pi = 0.60$ (see Fig. 5(e)) on account of the innate η_γ -factor.

Flux density and plaquette correlation. – To check the

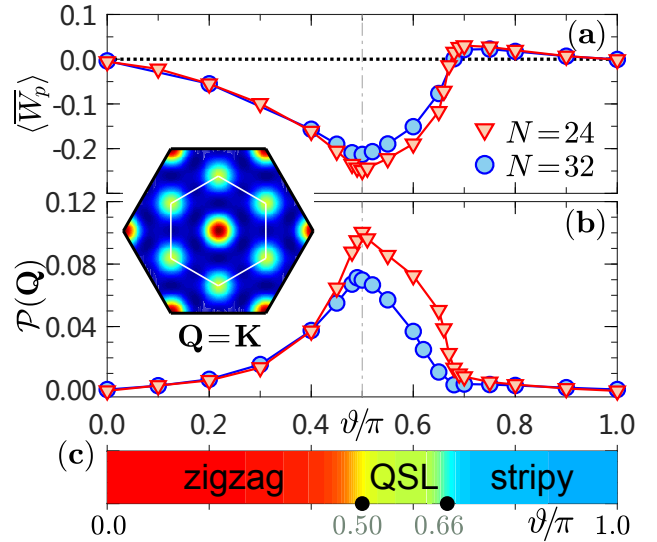


FIG. 6: (a) Flux density $\langle \bar{W}_p \rangle$ and (b) plaquette pseudo order parameter $\mathcal{P}(\mathbf{Q})$ for $N = 24$ (red triangular) and 32 (blue circle). Inset: visonic structure factor of HCGA. (c) Quantum phase diagram of the BMJF model on a honeycomb lattice.

topological excitations, we consider the hexagonal plaquette operator[11]

$$W_p = 2^6 \prod_{i \in p} S_i^\gamma = 2^6 S_1^x S_2^y S_3^z S_4^x S_5^y S_6^z, \quad (2)$$

which is the product of spin operators on out-going bonds around a plaquette (see Fig. 1(a)). Fig. 6(a) shows the flux density $\langle \bar{W}_p \rangle = \sum_p \langle W_p \rangle / N_p$ where $N_p = N/2$ is the number of hexagonal plaquette on clusters of $N = 24$ and 32 . Starting from $\vartheta/\pi = 0.0$, $\langle \bar{W}_p \rangle$ is zero, followed by a continuous decrease before arriving at the transition point, $\vartheta/\pi \simeq 0.50$. Afterwards, it begins to increase and then surpasses the critical line to enter into the stripy phase where $\langle \bar{W}_p \rangle > 0$. For HCGA we have $\langle \bar{W}_p \rangle = -0.25(2)$ [61], which is about a quarter of that in the Kitaev model[11]. We then introduce the plaquette pseudo order parameter $\mathcal{P}_{N_p}(\mathbf{Q})$ via the static visonic structure factor $\mathcal{W}_{N_p}(\mathbf{Q})$ [61]. From Fig. 6(b) we find that the QSL phase has a stable peak at Γ but a weaker intensity at \mathbf{K} point, signifying a perceptible plaquette correlation[61]. The entire quantum phase diagram of Eq. (1) is presented in Fig. 6(c). Apart from the conventional zigzag and stripy orders, there is a gapless QSL which sustains in a large region between $\vartheta_{t,l}$ and $\vartheta_{t,r}$ with $\vartheta_{t,l}/\pi \simeq 0.50$ and $\vartheta_{t,r}/\pi = 0.66(1)$. The ground state of HCGA locates at the leftmost transition point and is recognized as a QSL.

Summary and Discussion. – We have proposed and studied a BMJF model on a honeycomb lattice, of particular interest is an intermediate region sandwiched between the zigzag and stripy phases. Though exhibiting magnetic order at the classical level, quantum fluctuations disfavor such order since it acquires a large energy

according to LSWT. In the quantum case, it turns out to be a gapless QSL with a plaquette correlation, and is separated from its two neighbors by first-order transitions. More importantly, we take massive numerical efforts on HCFA and are able to confirm the following three physical issues. (i) The energy spectra collapse vividly on a $N = 24$ hexagonal cluster, and the empirical extrapolation on three large XC clusters gives a vanishing energy gap, in line with the logarithmic behaviors of entanglement entropy. (ii) Both the zigzag magnetic order and lattice nematic order vanish, consistent with the dramatic suppression of the magnetization of the zigzag order by LSWT. (iii) In the static visonic structure factor, there is a perceptible plaquette correlation because of a subleading peak at \mathbf{K} point. These findings strongly corroborate the nature of HCFA is a gapless QSL rather than a zigzag order, although the latter is close in energy. Our results clarify the controversy on HCFA and provide a significant guidance to further theoretical studies on the generic anisotropic model on a honeycomb lattice and to unveil the microscopic Hamiltonian that could describe the Kitaev material α - RuCl_3 .

Note added. – During the revision process, we became aware of a recent preprint[79], which confirms the non-magnetic nature of HCFA.

We thank S. Hu for many inspiring and fruitful discussions. We also thank M. Gohlke, J. S. Gordon, Y.-Z. Huang, T. Li, H.-J. Liao, K. Liu, Z.-X. Liu, B. Xi, and W. Yu for helpful discussions. J.Z. was supported by the the National Natural Science Foundation of China (Grant No. 11874188) and the Fundamental Research Funds for the Central Universities. H.-Y.K. was supported by the NSERC Discovery Grant No. 06089-2016. X.W. was supported by the National Program on Key Research Project (Grant No. 2016YFA0300501) and by the National Natural Science Foundation of China (Grants No. 11574200 and No. 11974244).

* zhaojz@lzu.edu.cn

† xiaoqunwang@sjtu.edu.cn

- [1] L. Balents, Nature (London) **464**, 199 (2010).
- [2] T.-H. Han, J. S. Helton, S. Chu, D. G. Nocera, J. A. Rodriguez-Rivera, C. Broholm, and Y. S. Lee, Nature (London) **492**, 406 (2012).
- [3] Y. Li, G. Chen, W. Tong, L. Pi, J. Liu, Z. Yang, X. Wang, and Q. Zhang, Phys. Rev. Lett. **115**, 167203 (2015).
- [4] H. J. Liao, Z. Y. Xie, J. Chen, Z. Y. Liu, H. D. Xie, R. Z. Huang, B. Normand, and T. Xiang, Phys. Rev. Lett. **118**, 137202 (2017).
- [5] K. W. Plumb, J. P. Clancy, L. J. Sandilands, V. V. Shankar, Y. F. Hu, K. S. Burch, H.-Y. Kee, and Y.-J. Kim, Phys. Rev. B **90**, 041112(R) (2014).
- [6] A. Banerjee, C. A. Bridges, J.-Q. Yan, A. A. Aczel, L. Li, M. B. Stone, G. E. Granroth, M. D. Lumsden, Y. Yiu, J. Knolle, S. Bhattacharjee, D. L. Kovrizhin, R. Moessner, D. A. Tennant, D. G. Mandrus, and S. E. Nagler, Nat. Mater. **15**, 733 (2016).
- [7] A. Banerjee, J. Yan, J. Knolle, C. A. Bridges, M. B. Stone, M. D. Lumsden, D. G. Mandrus, D. A. Tennant, R. Moessner, and S. E. Nagler, Science **356**, 1055 (2017).
- [8] J. G. Rau, E. K.-H. Lee, and H.-Y. Kee, Annu. Rev. Condens. Matter Phys. **7**, 195 (2016).
- [9] G. Jackeli and G. Khaliullin, Phys. Rev. Lett. **102**, 017205 (2009).
- [10] Z. Nussinov and J. van den Brink, Rev. Mod. Phys. **87**, 1 (2015).
- [11] A. Kitaev, Ann. Phys. **321**, 2 (2006).
- [12] F. Ye, S. Chi, H. Cao, B. C. Chakoumakos, J. A. Fernandez-Baca, R. Custelcean, T. F. Qi, O. B. Korneta, and G. Cao, Phys. Rev. B **85**, 180403(R) (2012).
- [13] S. K. Choi, R. Coldea, A. N. Kolmogorov, T. Lancaster, I. I. Mazin, S. J. Blundell, P. G. Radaelli, Y. Singh, P. Gegenwart, K. R. Choi, S.-W. Cheong, P. J. Baker, C. Stock, and J. Taylor, Phys. Rev. Lett. **108**, 127204 (2012).
- [14] S. H. Chun, J.-W. Kim, J. Kim, H. Zheng, C. C. Stoumpos, C. D. Malliakas, J. F. Mitchell, K. Mehlawat, Y. Singh, Y. Choi, T. Gog, A. Al-Zein, M. M. Sala, M. Krisch, J. Chaloupka, G. Jackeli, G. Khaliullin, and B. J. Kim, Nat. Phys. **11**, 462 (2015).
- [15] W. Wang, Z.-Y. Dong, S.-L. Yu, and J.-X. Li, Phys. Rev. B **96**, 115103 (2017).
- [16] J. A. Sears, M. Songvilay, K. W. Plumb, J. P. Clancy, Y. Qiu, Y. Zhao, D. Parshall, and Y.-J. Kim, Phys. Rev. B **91**, 144420 (2015).
- [17] I. A. Leahy, C. A. Pocs, P. E. Siegfried, D. Graf, S.-H. Do, K.-Y. Choi, B. Normand, and M. Lee, Phys. Rev. Lett. **118**, 187203 (2017).
- [18] J. A. Sears, Y. Zhao, Z. Xu, J. W. Lynn, and Y.-J. Kim, Phys. Rev. B **95**, 180411(R) (2017).
- [19] S.-H. Baek, S.-H. Do, K.-Y. Choi, Y. S. Kwon, A. U. B. Wolter, S. Nishimoto, J. van den Brink, and B. Büchner, Phys. Rev. Lett. **119**, 037201 (2017).
- [20] A. U. B. Wolter, L. T. Corredor, L. Janssen, K. Nenkov, S. Schönecker, S.-H. Do, K.-Y. Choi, R. Albrecht, J. Hunger, T. Doert, M. Vojta, and B. Büchner, Phys. Rev. B **96**, 041405(R) (2017).
- [21] Z. Wang, S. Reschke, D. Hüvonen, S.-H. Do, K.-Y. Choi, M. Gensch, U. Nagel, T. Room, and A. Loidl, Phys. Rev. Lett. **119**, 227202 (2017).
- [22] J. Zheng, K. Ran, T. Li, J. Wang, P. Wang, B. Liu, Z.-X. Liu, B. Normand, J. Wen, and W. Yu, Phys. Rev. Lett. **119**, 227208 (2017).
- [23] L. J. Sandilands, Y. Tian, K. W. Plumb, Y.-J. Kim, and K. S. Burch, Phys. Rev. Lett. **114**, 147201 (2015).
- [24] G. Li, X. Chen, Y. Gan, F. Li, M. Yan, F. Ye, S. Pei, Y. Zhang, L. Wang, H. Su, J. Dai, Y. Chen, Y. Shi, X. W. Wang, L. Zhang, S. Wang, D. Yu, F. Ye, J.-W. Mei, and M. Huang, Phys. Rev. Materials **3**, 023601 (2019).
- [25] S.-H. Do, S.-Y. Park, J. Yoshitake, J. Nasu, Y. Motome, Y. S. Kwon, D. T. Adroja, D. J. Voneshen, K. Kim, T.-H. Jang, J.-H. Park, K.-Y. Choi, and S. Ji, Nat. Phys. **13**, 1079 (2017).
- [26] K. Ran, J. Wang, W. Wang, Z.-Y. Dong, X. Ren, S. Bao, S. Li, Z. Ma, Y. Gan, Y. Zhang, J. T. Park, G. Deng, S. Danilkin, S.-L. Yu, J.-X. Li, and J. Wen, Phys. Rev. Lett. **118**, 107203 (2017).
- [27] S. M. Winter, K. Riedl, P. A. Maksimov, A. L. Chernyshev, A. Honecker, and R. Valentí, Nat. Commun. **8**,

- 1152 (2018).
- [28] H.-C. Jiang, Z.-C. Gu, X.-L. Qi, and S. Trebst, Phys. Rev. B **83**, 245104 (2011).
- [29] J. Nasu, M. Udagawa, and Y. Motome, Phys. Rev. B **92**, 115122 (2015).
- [30] L. Janssen, E. C. Andrade, and M. Vojta, Phys. Rev. Lett. **117**, 277202 (2016).
- [31] G.-W. Chern, Y. Sizyuk, C. Price, and N. B. Perkins, Phys. Rev. B **95**, 144427 (2017).
- [32] Z. Zhu, I. Kimchi, D. N. Sheng, and L. Fu, Phys. Rev. B **97**, 241110(R) (2018).
- [33] M. Gohlke, R. Moessner, and F. Pollmann, Phys. Rev. B **98**, 014418 (2018).
- [34] S. Liang, M.-H. Jiang, W. Chen, J.-X. Li, and Q.-H. Wang, Phys. Rev. B **98**, 054433 (2018).
- [35] J. Nasu, Y. Kato, Y. Kamiya, and Y. Motome, Phys. Rev. B **98**, 060416(R) (2018).
- [36] H.-C. Jiang, C.-Y. Wang, B. Huang, and Y.-M. Lu, [arXiv:1809.08247](https://arxiv.org/abs/1809.08247) (2018).
- [37] C. Hickey and S. Trebst, Nat. Commun. **10**, 530 (2019).
- [38] M. Hermanns, I. Kimchi, J. Knolle, Annu. Rev. Condens. Matter Phys. **9**, 17 (2018).
- [39] Y. D. Li, X. Yang, Y. Zhou, G. Chen, Phys. Rev. B **99**, 205119 (2019).
- [40] N. D. Patel and N. Trivedi, Proc. Natl. Acad. Sci. USA **116**, 12199 (2019).
- [41] L. Janssen, E. C. Andrade, and M. Vojta, Phys. Rev. B **96**, 064430 (2017).
- [42] P. Laurell and S. Okamoto, npj Quantum Materials **5**, 2 (2020).
- [43] P. A. Maksimov and A. L. Chernyshev, Phys. Rev. Research **2**, 033011 (2020).
- [44] J. G. Rau, E. K.-H. Lee, and H.-Y. Kee, Phys. Rev. Lett. **112**, 077204 (2014).
- [45] R. Yadav, N. A. Bogdanov, V. M. Katukuri, S. Nishimoto, J. van den Brink, and L. Hozoi, Sci. Rep. **6**, 37925 (2016).
- [46] Z.-X. Liu and B. Normand, Phys. Rev. Lett. **120**, 187201 (2018).
- [47] L. Zou and Y.-C. He, Phys. Rev. Research **2**, 013072 (2020).
- [48] G. Wachtel and D. Orgad, Phys. Rev. B **99**, 115104 (2019).
- [49] J. S. Gordon, A. Catuneanu, E. S. Sørensen, and H.-Y. Kee, Nat. Commun. **10**, 2470 (2019).
- [50] D. Takikawa and S. Fujimoto, Phys. Rev. B **99**, 224409 (2019).
- [51] P. Lampen-Kelley, S. Rachel, J. Reuther, J.-Q. Yan, A. Banerjee, C. A. Bridges, H. B. Cao, S. E. Nagler, D. Mandrus, Phys. Rev. B **98**, 100403(R) (2018).
- [52] A. M. Samarakoon, G. Wachtel, Y. Yamaji, D. A. Tennant, C. D. Batista, and Y. B. Kim, Phys. Rev. B **98**, 045121 (2018).
- [53] I. Rousochatzakis and N. B. Perkins, Phys. Rev. Lett. **118**, 147204 (2017).
- [54] A. Catuneanu, Y. Yamaji, G. Wachtel, Y.-B. Kim, and H.-Y. Kee, npj Quantum Materials **3**, 23 (2018).
- [55] M. Gohlke, G. Wachtel, Y. Yamaji, F. Pollmann, and Y. B. Kim, Phys. Rev. B **97**, 075126 (2018).
- [56] J. Wang, B. Normand, and Z.-X. Liu, Phys. Rev. Lett. **123**, 197201 (2019).
- [57] S. R. White, Phys. Rev. Lett. **69**, 2863 (1992).
- [58] E. M. Stoudenmire and S. R. White, Annu. Rev. Condens. Matter Phys. **3**, 111 (2012).
- [59] Z. Zhu, D. A. Huse, and S. R. White, Phys. Rev. Lett. **111**, 257201 (2013).
- [60] S.-S. Gong, D. N. Sheng, O. I. Motrunich, and M. P. A. Fisher, Phys. Rev. B **88**, 165138 (2013).
- [61] See Supplemental Material at [url] for configurations of classical phases and their LSWT calculation, DMRG details on the BMJF model, and scanning on a long but finite cylinder, which includes Refs. [62–66].
- [62] C. Liu, R. Yu, and X. Wang, Phys. Rev. B **94**, 174424 (2016).
- [63] Q. Luo, S. Hu, B. Xi, J. Zhao, and X. Wang, Phys. Rev. B **95**, 165110 (2017).
- [64] Z. Zhu, P. A. Maksimov, S. R. White, and A. L. Chernyshev, Phys. Rev. Lett. **119**, 157201 (2017).
- [65] Z. Zhu and S. R. White, Phys. Rev. B **92**, 041105(R) (2015).
- [66] W. Yang, A. Nocera, T. Tummuru, H.-Y. Kee, and I. Affleck, Phys. Rev. Lett. **124**, 147205 (2020).
- [67] N. Metropolis, A. W. Rosenbluth, M. N. Rosenbluth, A. H. Teller, and E. Teller, J. Chem. Phys. **21**, 1087 (1953).
- [68] K. Hukushima and K. Nemoto, J. Phys. Soc. Jpn. **65**, 1604 (1996).
- [69] L. Janssen and M. Vojta, J. Phys.: Condens. Matter **31**, 423002 (2019).
- [70] C. L. Henley, Phys. Rev. Lett. **62**, 2056 (1989).
- [71] Y.-Z. Huang, B. Xi, X. Chen, W. Li, Z.-C. Wang, and G. Su, Phys. Rev. E **93**, 062110 (2016).
- [72] Y.-Z. Huang and G. Su, Phys. Rev. E **95**, 052147 (2017).
- [73] The excitation gap of HCFM shows a pronounced size-dependent behavior, which is an evidence for a gapless ground state. The distinct difference between cylinders of $L_y = 3$ and $L_y = 4$ may imply a possible spinon Fermi surface spin liquid[61].
- [74] J. Eisert, M. Cramer, and M. B. Plenio, Rev. Mod. Phys. **82**, 277 (2010).
- [75] The full SMSF is defined as $\mathbb{S}_N(\mathbf{Q}) = \sum_{\alpha\beta} \delta_{\alpha\beta} \mathbb{S}_N^{\alpha\beta}(\mathbf{Q})$, where $\mathbb{S}_N^{\alpha\beta}(\mathbf{Q}) = \frac{1}{N} \sum_{ij} \langle S_i^\alpha S_j^\beta \rangle e^{i\mathbf{Q} \cdot (\mathbf{R}_i - \mathbf{R}_j)}$.
- [76] S.-S. Gong, W. Zhu, D. N. Sheng, and K. Yang, Phys. Rev. B **95**, 205132 (2017).
- [77] J.-Y. Chen, S. Capponi, and D. Poilblanc, Phys. Rev. B **98**, 045106 (2018).
- [78] P. Saha, Z. Fan, D. Zhang, and G.-W. Chern, Phys. Rev. Lett. **122**, 257204 (2019).
- [79] M. Gohlke, L. E. Chern, H.-Y. Kee, and Y. B. Kim, [arXiv:2003.11876](https://arxiv.org/abs/2003.11876).

Supplemental Material for “Gapless spin liquid state of the spin- $\frac{1}{2}$ honeycomb antiferromagnetic Γ model”

Qiang Luo^{1,2}, Jize Zhao³, Hae-Young Kee^{2,4}, and Xiaoqun Wang^{5,6}

¹*Department of Physics, Renmin University of China, Beijing 100872, China*

²*Department of Physics, University of Toronto, Toronto, Ontario M5S 1A7, Canada*

³*School of Physical Science and Technology & Key Laboratory for Magnetism and Magnetic Materials of the MoE, Lanzhou University, Lanzhou 730000, China*

⁴*Canadian Institute for Advanced Research, Toronto, Ontario, M5G 1Z8, Canada*

⁵*Key Laboratory of Artificial Structures and Quantum Control (Ministry of Education), School of Physics and Astronomy, Tsung-Dao Lee Institute, Shanghai Jiao Tong University, Shanghai 200240, China*

⁶*Beijing Computational Science Research Center, Beijing 100084, China*

CONFIGURATIONS OF CLASSICAL PHASES

Ground state of the classical Γ model

For the classical phase diagram of the bond-modulated J - Γ (BMJ Γ) model considered in the main text (see Eq. (1)), the ground state of the *classical* Γ model locates at the transition point between the zigzag phase and the mixed phase. Such a ground state is known to be a classical spin liquid with a macroscopic ground-state degeneracy[1]. In particular, Roussochatzakis and Perkins parameterize the classical spin as $\mathbf{S}_n = (\eta_i a, \eta_j b, \eta_k c)$ where $a = |S_n^x|$ ($\eta_i = \text{sgn}(S_n^x)$), $b = |S_n^y|$ ($\eta_j = \text{sgn}(S_n^y)$), and $c = |S_n^z|$ ($\eta_k = \text{sgn}(S_n^z)$). Here, $\sqrt{a^2 + b^2 + c^2} = S$ and $\eta_i = \pm 1$ are Ising variables. The choice of η 's accounts for the ground-state degeneracy for any specific $\{a, b, c\}$. For a N -site honeycomb lattice, the number of η 's is $N/2$ (i.e., equal to that of hexagons) and thus the degeneracy of the ground state is $2^{N/2}$ [1]. Many conventional magnetic orders, such as two-sublattice Néel order, four-sublattice zigzag order, and six-sublattice 120° order, contribute to the large family of the classical ground-state manifold[2]. The typical static magnetic structure factor (SMSF) is shown in Fig. SM-1 and it is featureless, signalling the spin liquid nature.

As shown in the main text, the ground-state energy per site e_g is exactly -1 . The exact result could also be obtained by the Luttinger-Tisza method. This method not only gives the lowest bound of the energy, but also shows that all the energy bands in the reciprocal space are completely flat, which is a reminiscence of the highly frustrated nature of the Γ model[1]. Meanwhile, to study the finite-size scaling of the energy, we calculate the classical energy at several different sizes. Here, both cylindrical boundary condition (CBC) and toroidal boundary condition (TBC) are utilized but with different aspect ratio L_x/L_y , which is 2 for the former and 1 for the latter. It could be observed in Fig. SM-1 that the energy e_g does not show any finite-size effect under TBC, while it obeys a linear scaling law under CBC. In the thermodynamic limit, it is -1 for both cases.

The classical ground states of the negative Γ model on the honeycomb lattice can be obtained by time reversal operation in every second lattice site[1]. In this case, its ground state is also a classical spin liquid. Unlike the classical ground state of the (anti-)ferromagnetic Heisenberg model where all the spins on the neighboring two sublattices are (anti-)parallel, the terminology of ferromagnetic/antiferromagnetic Γ model is more or less not very straightforward. However, it is legitimate for us to have such a nomenclature by noticing that the Neel order is one of the degenerate ground states of the positive Γ model, while the ferromagnetic order is not. Therefore, it is reasonable for one to call the antiferromagnetic Γ model without any ambiguity. A similar situation also suits for the negative case.

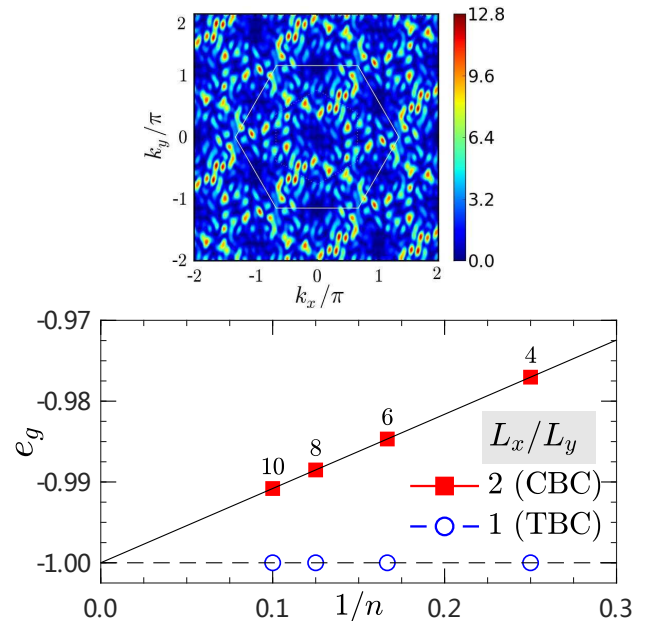


FIG. SM-1: Upper panel: Typical SMSF of the classical Γ model with the system size $L_x \times L_y = 16 \times 16$. Lower panel: Classical energy e_g of the Γ model under CBC with $L_x/L_y = 2$ (red square) and TBC with $L_x/L_y = 1$ (blue circle).

The zigzag and stripy phases

In this part we will go into the zigzag and stripy phases shown in Fig. 1 of the main text. The zigzag order can be described as ferromagnetic zigzag chains coupled antiferromagnetically. The stripe order, on the contrary, is formed by antiferromagnetic zigzag chains with ferromagnetic coupling. Both phases could be divided into two sublattices with opposite spins. The classical spin, which is an $O(3)$ vector, can be written as

$$\mathbf{S}_i = S (\sin \theta_i \cos \phi_i, \sin \theta_i \sin \phi_i, \cos \theta_i), \quad (\text{SM-1})$$

where $\theta_i \in [0, \pi)$ and $\phi_i \in [0, 2\pi)$ are respectively the polar and azimuthal angles at site i . Suppose that one sublattice has the angles (θ, ϕ) , then the other sublattice has the angles $(\pi - \theta, \pi + \phi)$. The three bonds (i.e., \mathbf{X} , \mathbf{Y} , and \mathbf{Z} bonds) have different contributions to the total energy and should be considered separately. After adding up all the terms, we find that the energies per site in the two phases are

$$e_g^{\text{zigzag}} = -\frac{1}{2}(3J + \mathcal{F}_{\max}(\theta, \phi)\Gamma) \quad (\text{SM-2})$$

and

$$e_g^{\text{stripy}} = \frac{1}{2}(3J + \mathcal{F}_{\min}(\theta, \phi)\Gamma) \quad (\text{SM-3})$$

where an auxiliary function $\mathcal{F}(\theta, \phi)$ is introduced naturally. It is worth mentioning that whereas Γ is always nonnegative, the Heisenberg interaction J is positive (negative) in the zigzag (stripy) phase. The explicit form of the function is

$$\mathcal{F}(\theta, \phi) = \sin^2 \theta \sin 2\phi - \sin 2\theta(\sin \phi + \cos \phi). \quad (\text{SM-4})$$

Its maximum is 2 with $(\theta, \phi) = (\pi - \text{atan}(\sqrt{2}), \pi/4)$ or $(\theta, \phi) = (\text{atan}(\sqrt{2}), 5\pi/4)$ and its minimum is -1 , see Fig. SM-2. All the critical points are given by the following identify

$$\tan 2\theta = \frac{1}{\sin \phi} + \frac{1}{\cos \phi}. \quad (\text{SM-5})$$

The classical energy of the zigzag phase is $e_g^{\text{zigzag}} = -(2\Gamma + 3J)/2$, and the angles of the spins are either $(\theta, \phi) = (\pi - \text{atan}(\sqrt{2}), \pi/4)$ or $(\theta, \phi) = (\text{atan}(\sqrt{2}), 5\pi/4)$. In other words, the classical magnetic direction $\mathbf{n} = \frac{1}{\sqrt{3}}(\mathbf{e}_x + \mathbf{e}_y - \mathbf{e}_z)$, or $\mathbf{n} = [11\bar{1}]$ for short. Interestingly, the three components of the spin vector have an equal strength of $\sqrt{3}/3$. The energy of the stripy phase is $e_g^{\text{stripy}} = -(\Gamma - 3J)/2$, and the angles satisfy the restriction Eq. (SM-5). Its moment direction is free to vary in the plane that is perpendicular to \mathbf{n} . Since there are infinite solutions to Eq. (SM-5) which span in a certain locus as shown in Fig. SM-2, we conclude that there is an emergent continuous symmetry in the classical stripy phase.

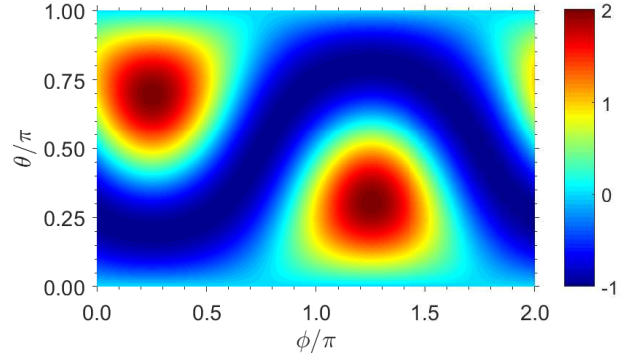


FIG. SM-2: Illustration of function $\mathcal{F}(\theta, \phi)$ (see Eq. (SM-4)) in the whole parameter region.

The mixed AFM–twining zigzag phase

Due to the bond-modulated $\eta_{ij}(\pm 1)$ term, the BMJF model does not possess C_6 rotational symmetry. Therefore, three degenerate configurations of the zigzag order does not apply here. We find that the other two twining zigzag orders (see Fig. SM-3(b) and (c)) have higher energy than the zigzag order (see Fig. 1(c) of the main text) when $\vartheta/\pi \in [0, 1/2)$. When ϑ/π is slightly larger than $1/2$, the twining zigzag orders overcome the latter and become the ground state. Interestingly, the AFM order (see Fig. SM-3(a)) has the same energy and contributes to the degenerate manifolds. Moreover, due to the two nonequivalent sites per unit cell, each configuration is two-fold degenerate. Consequently, we conclude that the mixed phase has six-fold degenerate ground states.

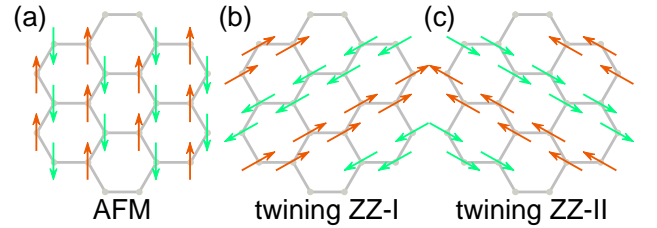


FIG. SM-3: The degenerate ground states of the mixed phase, which includes (a) AFM order and (b)/(c) two kinds of twining zigzag orders.

The energy of the mixed phase is given by

$$e_g^{\text{mixed}} = -\frac{1}{2}(-J + \mathcal{F}_{\max}(\theta, \phi + \pi)\Gamma). \quad (\text{SM-6})$$

Since the translation of ϕ by π does not change the magnitude of the function $\mathcal{F}(\theta, \phi)$, we then obtain $e_g^{\text{mixed}} = -(2\Gamma - J)/2$ with $(\theta, \phi) = (\text{atan}(\sqrt{2}), \pi/4)$ or $(\theta, \phi) = (\pi - \text{atan}(\sqrt{2}), 5\pi/4)$. In this case the classical magnetic direction $\mathbf{n} = [111]$.

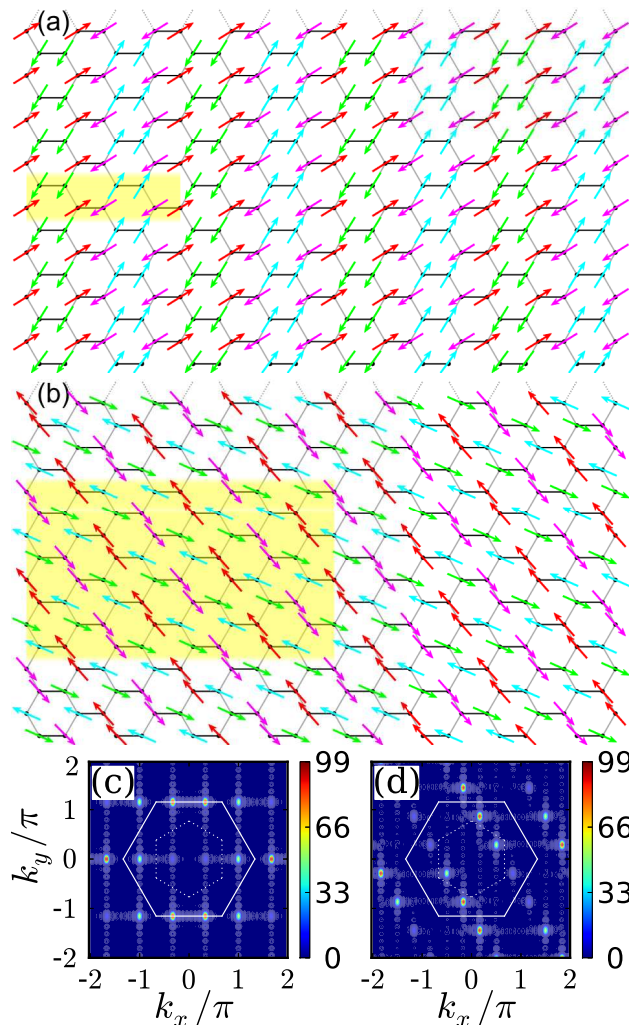


FIG. SM-4: Configurations of the noncollinear phase in the real space. The size of the unit cell marked by the yellow shadow is (a) 4×2 and (b) 8×8 . Their SMSFs in the momentum space are shown in (c) and (d), respectively.

The noncollinear phase

In addition to the zigzag phase, the stripy phase, and the mixed phase discussed above, there is a noncollinear (NCL) phase consisting of two kinds of spins (or four if we consider that two of them are anti-parallel to their partners) which are neither (anti-)parallel nor perpendicular in the classical phase diagram. Suppose that the angles of one kind of the spins are (θ, ϕ) , then they are $(\theta + \pi/2, \phi + \pi)$ for the other. Namely,

$$\begin{cases} \mathbf{S}_a = S (\sin \theta \cos \phi, \sin \theta \sin \phi, \cos \theta) \\ \mathbf{S}_b = -S (\cos \theta \cos \phi, \cos \theta \sin \phi, \sin \theta) \end{cases}. \quad (\text{SM-7})$$

One of the configurations of the spins is shown in Fig. SM-4(a). The optimal angles could be obtained by minimizing the classical energy

$$e_g^{\text{NCL}} = J \sin 2\theta + \frac{\Gamma}{4} [\cos 2\theta \sin 2\phi - 2(\sin \phi + \cos \phi)]. \quad (\text{SM-8})$$

For example, if $\theta = 3\pi/4 - \psi_0/2$ and $\phi = \pi/4$ where $\psi_0 = \text{atan}(\frac{\Gamma}{4J})$, we have the classical energy

$$e_g^{\text{NCL}} = -\sqrt{J^2 + \frac{\Gamma^2}{16}} - \frac{\Gamma}{\sqrt{2}}. \quad (\text{SM-9})$$

We also note that the angles between the two kinds of spins are $-\psi_0$ or its supplementary angle $\pi + \psi_0$. Since ψ_0 is ϑ -dependent, the polar angle θ also varies with ϑ .

The fascinating character of the NCL phase is that it may also possess other ground states with larger unit cell. For example, we find such a ground state whose unit cell has 64 lattice sites, see Fig. SM-4(b).

QUANTUM FLUCTUATIONS IN THE LINEAR SPIN-WAVE THEORY

The classical analysis in the preceding section gives the classical magnetic orders of the whole system. In this section, we go beyond the classical level by considering the quantum fluctuations to find out where the nonmagnetic state may appear in the phase diagram. To this end, we utilize the linear spin-wave theory (LSWT) where each local spin operator $\mathbf{S}_i = (S_i^x, S_i^y, S_i^z)$ is represented by bosonic creation and annihilation operators a_i and a_i^\dagger . We follow essentially the frame by Janssen and Vojta[3]. By virtue of the Holstein-Primakoff transformation,

$$\begin{aligned} \tilde{S}_i^+ &= \sqrt{2S} \sqrt{1 - \frac{a_i^\dagger a_i}{2S}} a_i = \sqrt{2S} a_i + \mathcal{O}(1/\sqrt{S}), \\ \tilde{S}_i^- &= \sqrt{2S} a_i^\dagger \sqrt{1 - \frac{a_i^\dagger a_i}{2S}} = \sqrt{2S} a_i^\dagger + \mathcal{O}(1/\sqrt{S}), \\ \tilde{S}_i^z &= S - a_i^\dagger a_i. \end{aligned} \quad (\text{SM-10})$$

Here, $\tilde{S}_i^n \equiv (\mathbf{S} \cdot \mathbf{n})$ is the spin component along the classical ordered moment \mathbf{n} and $\tilde{S}_i^\pm \equiv (\mathbf{S}_i \cdot \mathbf{e}) \pm i[\mathbf{S}_i \cdot (\mathbf{n} \times \mathbf{e})]$ are the ladder operators consisting of the orthogonal spin components, with \mathbf{e} being an (arbitrary) unit vector perpendicular

to \mathbf{n} and satisfying the right-hand rule. The spin operator is thus

$$\mathbf{S}_{\tau,i} = \sqrt{\frac{S}{2}}(a_i + a_i^\dagger)\mathbf{e} + \tau\sqrt{\frac{S}{2}}(-ia_i + ia_i^\dagger)(\mathbf{n} \times \mathbf{e}) + \tau(S - a_i^\dagger a_i)\mathbf{n} \quad (\text{SM-11})$$

where τ is introduced for classical spin which is either parallel ($\tau = +1$) or antiparallel ($\tau = -1$) to \mathbf{n} . For each γ -component $S_{\tau,i}^\gamma = \mathbf{S}_i \cdot \mathbf{e}_\gamma$, we have

$$\begin{aligned} S_{\tau,i}^\gamma &= \sqrt{\frac{S}{2}}a_i(\mathbf{e} \cdot \mathbf{e}_\gamma - \nu\tau(\mathbf{n} \times \mathbf{e}) \cdot \mathbf{e}_\gamma) + \sqrt{\frac{S}{2}}a_i^\dagger(\mathbf{e} \cdot \mathbf{e}_\gamma + \nu\tau(\mathbf{n} \times \mathbf{e}) \cdot \mathbf{e}_\gamma) + \tau(S - a_i^\dagger a_i)(\mathbf{n} \cdot \mathbf{e}_\gamma) \\ &= \sqrt{\frac{S}{2}}a_i(\xi^\gamma - \nu\tau\eta^\gamma) + \sqrt{\frac{S}{2}}a_i^\dagger(\xi^\gamma + \nu\tau\eta^\gamma) + \tau(S - a_i^\dagger a_i)\zeta^\gamma \end{aligned} \quad (\text{SM-12})$$

where $\xi^\gamma = \mathbf{e} \cdot \mathbf{e}_\gamma$, $\eta^\gamma = (\mathbf{n} \times \mathbf{e}) \cdot \mathbf{e}_\gamma$, and $\zeta^\gamma = \mathbf{n} \cdot \mathbf{e}_\gamma$. Before going into detail, we shall define an auxiliary function

$$\mathcal{G}_\tau^{\alpha\beta}(x) = (\xi^\alpha \xi^\beta + x\eta^\alpha \eta^\beta) + \nu\tau \frac{1-x}{2}(\xi^\alpha \eta^\beta + \xi^\beta \eta^\alpha), \quad (\text{SM-13})$$

which satisfies $\mathcal{G}_{-\tau}^{\alpha\beta}(x) = [\mathcal{G}_\tau^{\alpha\beta}(x)]^*$. Specifically, $\mathcal{G}_\tau^{\alpha\beta}(1) = \mathcal{G}_\pm^{\alpha\beta}(1) = \xi^\alpha \xi^\beta + \eta^\alpha \eta^\beta$ and $\mathcal{G}_{\tau=-1}^{\alpha\beta}(-1) = (\xi^\alpha + \nu\eta^\alpha)(\xi^\beta + \nu\eta^\beta) = [\mathcal{G}_{\tau=-1}^{\alpha\beta}(-1)]^*$.

four-sublattice zigzag order

For the Hamiltonian shown in Eq. (1) of the main text, we can split it into two parts by the four kinds of sites (namely, the sublattice number $n_s = 4$; $N_s = N/n_s$) shown in Fig. 1(a) of the main text,

$$\mathcal{H} = \sum_{i \in \mathcal{A}} \mathcal{H}_\mathcal{A} + \sum_{j \in \mathcal{C}} \mathcal{H}_\mathcal{C}. \quad (\text{SM-14})$$

For any bond $\langle ij \rangle_\gamma$ bond, we shall define $\tau_\gamma = \tau\tau'$ where τ (τ') is a signal for site i (j). Essentially, for the zigzag order we have $\tau_\gamma = -\eta_\gamma$ where the latter is the bond-modulated factor for the Heisenberg interaction. To begin with, let us now concentrate on the \mathcal{A} -sublattice, which results in

$$\begin{aligned} \mathcal{H}_\mathcal{A} &= -N_s S^2 [3J - 2\Gamma(\zeta^y \zeta^z + \zeta^z \zeta^x - \zeta^x \zeta^y)] \\ &\quad + S \sum_{\mathbf{q}} \left\{ [3J - 2\Gamma(\zeta^y \zeta^z + \zeta^z \zeta^x - \zeta^x \zeta^y)] a_{\mathbf{q}}^\dagger a_{\mathbf{q}} + [2J - 2\Gamma(\zeta^y \zeta^z + \zeta^z \zeta^x)] d_{\mathbf{q}}^\dagger d_{\mathbf{q}} \right. \\ &\quad \left. + (J + 2\Gamma\zeta^x \zeta^y) b_{\mathbf{q}}^\dagger b_{\mathbf{q}} \right\} \\ &\quad + S \sum_{\mathbf{q}} \left\{ \left[-J(e^{i\mathbf{q}\delta_x} + e^{i\mathbf{q}\delta_y}) + \Gamma(\mathcal{G}_{\tau=1}^{yz}(1)e^{i\mathbf{q}\delta_x} + \mathcal{G}_{\tau=1}^{zx}(1)e^{i\mathbf{q}\delta_y}) \right] a_{\mathbf{q}}^\dagger d_{\mathbf{q}} \right. \\ &\quad \left. + \Gamma\mathcal{G}_{\tau=1}^{xy}(-1)e^{i\mathbf{q}\delta_z} a_{\mathbf{q}}^\dagger b_{\mathbf{q}} \right\} + \text{h.c.} \\ &\quad + S \sum_{\mathbf{q}} \Gamma(\mathcal{G}_{\tau=1}^{yz}(-1)e^{i\mathbf{q}\delta_x} + \mathcal{G}_{\tau=1}^{zx}(-1)e^{i\mathbf{q}\delta_y}) a_{\mathbf{q}}^\dagger d_{-\mathbf{q}}^\dagger + (J + \Gamma\mathcal{G}_{\tau=1}^{xy}(1))e^{i\mathbf{q}\delta_z} a_{\mathbf{q}}^\dagger b_{-\mathbf{q}}^\dagger + \text{h.c.} \end{aligned} \quad (\text{SM-15})$$

where $\delta_x = (-\frac{a_\square}{6}, \frac{b_\square}{2})$, $\delta_y = (-\frac{a_\square}{6}, -\frac{b_\square}{2})$, and $\delta_z = (\frac{a_\square}{3}, 0)$. Here, $a_\square \times b_\square$ is the unit cell of the zigzag order, see Fig. 1(a) of the main text. For the \mathcal{C} -sublattice, we in fact do not need to perform the tedious calculation, but instead use the following substitution:

$$a \Leftrightarrow c, \quad b \Leftrightarrow d, \quad \text{and} \quad \tau \Leftrightarrow -\tau. \quad (\text{SM-16})$$

Taken together, we arrive at the following spin-wave Hamiltonian

$$\begin{aligned} \mathcal{H}_\mathcal{T} &= -2N_s S(S+1) [3J - 2\Gamma(\zeta^y \zeta^z + \zeta^z \zeta^x - \zeta^x \zeta^y)] \\ &\quad + \frac{S}{2} \sum_{\mathbf{q}} \hat{\mathbf{x}}_{\mathbf{q}}^\dagger \hat{\mathbf{H}}_{\mathbf{q}} \hat{\mathbf{x}}_{\mathbf{q}}. \end{aligned} \quad (\text{SM-17})$$

where $\hat{\mathbf{x}}_{\mathbf{q}}^\dagger = (a_{\mathbf{q}}^\dagger, b_{\mathbf{q}}^\dagger, c_{\mathbf{q}}^\dagger, d_{\mathbf{q}}^\dagger, a_{-\mathbf{q}}, b_{-\mathbf{q}}, c_{-\mathbf{q}}, d_{-\mathbf{q}})$ is a vector of length $2n_s$ and $\hat{\mathbf{H}}_{\mathbf{q}}$ is a $2n_s \times 2n_s$ matrix of the form

$$\hat{\mathbf{H}}_{\mathbf{q}} = \begin{pmatrix} \hat{\Lambda}_{\mathbf{q}} & \hat{\Delta}_{\mathbf{q}} \\ \hat{\Delta}_{\mathbf{q}}^\dagger & \hat{\Lambda}_{-\mathbf{q}}^T \end{pmatrix} \quad (\text{SM-18})$$

with

$$\hat{\Lambda}_{\mathbf{q}} = \begin{pmatrix} A & E_{\mathbf{q}} & \circ & B_{\mathbf{q}} \\ E_{\mathbf{q}}^* & A & B_{\mathbf{q}}^* & \circ \\ \circ & B_{\mathbf{q}} & A & E_{\mathbf{q}} \\ B_{\mathbf{q}}^* & \circ & E_{\mathbf{q}}^* & A \end{pmatrix}, \quad \hat{\Delta}_{\mathbf{q}} = \begin{pmatrix} \circ & C_{\mathbf{q}} & \circ & D_{\mathbf{q},+} \\ C_{\mathbf{q}}^* & \circ & D_{\mathbf{q},+}^* & \circ \\ \circ & D_{\mathbf{q},-} & \circ & C_{\mathbf{q}} \\ D_{\mathbf{q},-}^* & \circ & C_{\mathbf{q}}^* & \circ \end{pmatrix}. \quad (\text{SM-19})$$

Those matrix entries are given by

$$\begin{cases} A = 3J - 2\Gamma(\zeta^y\zeta^z + \zeta^z\zeta^x - \zeta^x\zeta^y) \\ B_{\mathbf{q}} = -J(e^{i\mathbf{q}\delta_x} + e^{i\mathbf{q}\delta_y}) + \Gamma[\mathcal{G}^{yz}(1)e^{i\mathbf{q}\delta_x} + \mathcal{G}^{zx}(1)e^{i\mathbf{q}\delta_y}] \\ C_{\mathbf{q}} = [J + \Gamma\mathcal{G}^{xy}(1)]e^{i\mathbf{q}\delta_z} \\ D_{\mathbf{q},\tau} = \Gamma[\mathcal{G}_\tau^{yz}(-1)e^{i\mathbf{q}\delta_x} + \mathcal{G}_\tau^{zx}(-1)e^{i\mathbf{q}\delta_y}] \\ E_{\mathbf{q},\tau} = \Gamma\mathcal{G}_\tau^{xy}(-1)e^{i\mathbf{q}\delta_z} \end{cases}. \quad (\text{SM-20})$$

In what follows we shall make a simplification by choosing the proper crystalline axis. Motivated by the classical analysis in the last Section, we have $\mathbf{e} = [112]$, $\mathbf{n} \times \mathbf{e} = [1\bar{1}0]$, and $\mathbf{n} = [11\bar{1}]$, then we have

$$[\zeta_\alpha\zeta_\beta] = \frac{1}{3} \begin{pmatrix} 1 & 1 & -1 \\ 1 & 1 & -1 \\ -1 & -1 & 1 \end{pmatrix}, \quad [\mathcal{G}^{\alpha\beta}(1)] = \frac{1}{3} \begin{pmatrix} 2 & -1 & 1 \\ -1 & 2 & 1 \\ 1 & 1 & 2 \end{pmatrix}, \quad [\mathcal{G}_{\tau=1}^{\alpha\beta}(-1)] = \frac{2}{3} \begin{pmatrix} \omega & 1 & -\omega^{-1} \\ 1 & \omega^{-1} & -\omega \\ -\omega^{-1} & -\omega & 1 \end{pmatrix} \quad (\text{SM-21})$$

where $\omega = e^{2\pi i/3}$. parameterizing the wave vector \mathbf{q} in units of (h, k) as $\mathbf{q} = (\frac{2\pi}{a_\square}h, \frac{2\pi}{b_\square}k)[4]$, we have

$$\begin{cases} A = 3J + 2\Gamma \\ B_{\mathbf{q}} = -2(J - \Gamma/3)\varrho^{-1} \cos \pi k \\ C_{\mathbf{q}} = (J - \Gamma/3)\varrho^2 \\ D_{\mathbf{q},\tau} = \frac{2\Gamma}{3}(\cos \pi k + \tau\sqrt{3} \sin \pi k)\varrho^{-1} \\ E_{\mathbf{q}} = \frac{2\Gamma}{3}\varrho^2 \end{cases}. \quad (\text{SM-22})$$

where $\varrho = e^{i\pi h/3}$. It could be proved that $B_{-\mathbf{q}} = B_{\mathbf{q}}^*$, $C_{-\mathbf{q}} = C_{\mathbf{q}}^*$, $E_{-\mathbf{q}} = E_{\mathbf{q}}^*$, and $D_{-\mathbf{q},\tau} = D_{\mathbf{q},-\tau}^*$. This imply that $\hat{\Lambda}_{\mathbf{q}}^\dagger = \hat{\Lambda}_{\mathbf{q}}$ and $\hat{\Delta}_{-\mathbf{q}}^T = \hat{\Delta}_{\mathbf{q}}^\dagger$.

The quadratic Hamiltonian Eq. (SM-17) can be diagonalized via a bosonic Bogoliubov transformation[3],

$$\begin{pmatrix} \Omega(\mathbf{q}) & 0 \\ 0 & \Omega(\mathbf{q}) \end{pmatrix} = T^\dagger(\mathbf{q}) \begin{pmatrix} \hat{\Lambda}_{\mathbf{q}} & \hat{\Delta}_{\mathbf{q}} \\ \hat{\Delta}_{\mathbf{q}}^\dagger & \hat{\Lambda}_{-\mathbf{q}}^T \end{pmatrix} T(\mathbf{q}) \quad (\text{SM-23})$$

where $\Omega(\mathbf{q}) = \text{diag}(\omega_{\mathbf{q},1}, \omega_{\mathbf{q},2}, \dots, \omega_{\mathbf{q},n_s})$. The transformation matrix satisfies the orthogonality relations $T\Sigma T^\dagger = T^\dagger\Sigma T = \Sigma$ where $\Sigma = \text{diag}(\mathbb{1}, -1)$. The spectrum of the Hamiltonian can be obtained by the eigenvalue equation

$$\begin{pmatrix} \hat{\Lambda}_{\mathbf{q}} & \hat{\Delta}_{\mathbf{q}} \\ -\hat{\Delta}_{\mathbf{q}}^\dagger & -\hat{\Lambda}_{-\mathbf{q}}^T \end{pmatrix} \begin{pmatrix} \vec{u}_{\mathbf{q}}^{(n)} \\ \vec{v}_{-\mathbf{q}}^{*(n)} \end{pmatrix} = \omega_{\mathbf{q},n} \begin{pmatrix} \vec{u}_{\mathbf{q}}^{(n)} \\ \vec{v}_{-\mathbf{q}}^{*(n)} \end{pmatrix}. \quad (\text{SM-24})$$

If the eigenvector $|n(\mathbf{q})\rangle \equiv (\vec{u}_{\mathbf{q}}^{(n)}, \vec{v}_{-\mathbf{q}}^{*(n)})^T$ is normalized with respect to the inner product involving the matrix Σ , i.e., $\langle n(\mathbf{q})|\Sigma|n(\mathbf{q})\rangle = 1$ with $\langle n(\mathbf{q})| \equiv |n(\mathbf{q})\rangle^\dagger$, then the columns of the matrix $T(\mathbf{q})$ are given by the two vectors $|n(\mathbf{q})\rangle$.

In addition to the spin-wave dispersion relations which are usually of prime interest, there are also two other important quantities which can easily be calculated using LSWT. Namely, (i) the value of the total ordered moment $\langle M \rangle$ per site, and (ii) the total energy per site ε . For the classical moment $\langle M \rangle$, it is straightforwardly to get[3]

$$\begin{aligned} \frac{M}{S} &= \frac{1}{N_s n_s} \sum_{\{i\} \in N_s} \sum_{\{s\} \in n_s} \left(1 - \frac{1}{S} \langle a_{i,s}^\dagger a_{i,s} \rangle\right) + \mathcal{O}(1/S^2) \\ &= 1 - \frac{1}{n_s S} \sum_{\{s\} \in n_s} \int \frac{d^2\mathbf{q}}{(2\pi)^2} |\vec{v}_{-\mathbf{q}}^{*(n)}|^2 + \mathcal{O}(1/S^2), \end{aligned} \quad (\text{SM-25})$$

where $v_{-\mathbf{q}}^{*(n)}$ denotes the lower half of the normalized n -th eigenvector occurring in Eq. (SM-24), with positive energy $\omega_{\mathbf{q},n}$. The momentum integral is over all wavevectors $\mathbf{q} = (q_x, q_y)$ in the Brillouin zone. Likewise, the spin wave energy ε is given by[3]

$$\varepsilon = S(S+1)\varepsilon_{\text{cl}} + \frac{S}{2n_s} \sum_{\{s\} \in n_s} \int \frac{d^2\mathbf{q}}{(2\pi)^2} \omega_{\mathbf{q},n} + \mathcal{O}(1/S^2). \quad (\text{SM-26})$$

four-sublattice stripy order

Like the zigzag order, the stripy order also has four sublattices. The difference lies in that for the stripy order we have $\tau_\gamma = \eta_\gamma$. Following a very similar procedure, we get the spin-wave Hamiltonian for the stripy order as

$$\begin{aligned} \mathcal{H}_\mathcal{T} &= 2N_s S(S+1) [3J - 2\Gamma(\zeta^y \zeta^z + \zeta^z \zeta^x - \zeta^x \zeta^y)] \\ &+ \frac{S}{2} \sum_{\mathbf{q}} \hat{\mathbf{x}}_{\mathbf{q}}^\dagger \hat{\mathbf{H}}_{\mathbf{q}} \hat{\mathbf{x}}_{\mathbf{q}}. \end{aligned} \quad (\text{SM-27})$$

$\hat{\mathbf{H}}_{\mathbf{q}}$ is a $2n_s \times 2n_s$ matrix of the same form of Eq. (SM-18), but the entries are different, with

$$\hat{\Lambda}_{\mathbf{q}} = \begin{pmatrix} A & E_{\mathbf{q}} & \circ & B_{\mathbf{q},+} \\ E_{\mathbf{q}}^* & A & B_{\mathbf{q},-}^* & \circ \\ \circ & B_{\mathbf{q},-} & A & E_{\mathbf{q}} \\ B_{\mathbf{q},+}^* & \circ & E_{\mathbf{q}}^* & A \end{pmatrix}, \quad \hat{\Delta}_{\mathbf{q}} = \begin{pmatrix} \circ & C_{\mathbf{q},+} & \circ & D_{\mathbf{q}} \\ C_{-\mathbf{q},+} & \circ & D_{-\mathbf{q}} & \circ \\ \circ & D_{\mathbf{q}} & \circ & C_{\mathbf{q},-} \\ D_{-\mathbf{q}} & \circ & C_{-\mathbf{q},-} & \circ \end{pmatrix}. \quad (\text{SM-28})$$

Those matrix entries are given by

$$\begin{cases} A = 2\Gamma(\zeta^y \zeta^z + \zeta^z \zeta^x - \zeta^x \zeta^y) - 3J \\ B_{\mathbf{q},\tau} = \Gamma(\mathcal{G}_\tau^{yz}(-1)e^{i\mathbf{q}\delta_x} + \mathcal{G}_\tau^{zx}(-1)e^{i\mathbf{q}\delta_y}) \\ C_{\mathbf{q},\tau} = \Gamma\mathcal{G}_\tau^{xy}(-1)e^{i\mathbf{q}\delta_z} \\ D_{\mathbf{q}} = -J(e^{i\mathbf{q}\delta_x} + e^{i\mathbf{q}\delta_y}) + \Gamma(\mathcal{G}^{yz}(1)e^{i\mathbf{q}\delta_x} + \mathcal{G}^{zx}(1)e^{i\mathbf{q}\delta_y}) \\ E_{\mathbf{q}} = [J + \Gamma\mathcal{G}^{xy}(1)]e^{i\mathbf{q}\delta_z} \end{cases}. \quad (\text{SM-29})$$

As shown in the last Section, there is an emergent continuous $U(1)$ symmetry for the stripy order. The spins are perpendicular to \mathbf{c} [$11\bar{1}$], but could vary freely in the plane spanned by \mathbf{a} [112] and \mathbf{b} [$1\bar{1}0$]. Due to the quantum fluctuations, the degeneracy is usually lifted via order-by-disorder mechanism, selecting the two stripy order that break rotational lattice symmetry. To illustrate it, we firstly define the quantum energy correction $\Delta E(\phi) = S\varepsilon_{\text{cl}} + \frac{S}{2n_s} \sum_{\{s\} \in n_s} \int \frac{d^2\mathbf{q}}{(2\pi)^2} \omega_{\mathbf{q},n}(\phi)$, where ϕ is the angle between \mathbf{a} and \mathbf{b} . For $\vartheta/\pi = 0.75$, which is deep in the stripy order, we shows the $\Delta E(\phi)$ vs ϕ in the inset of Fig. SM-5. It is found that the energy correction has its minima at $\phi = 0$ or π , corresponding the two mostly favored configurations in the quantum level. The energy barrier, δE , defined as the energy difference between $\Delta E(\pi/2)$ and $\Delta E(0)$, is approximately 0.0175. The main part of Fig. SM-5 is the whole energy barrier at different ϑ/π in the stripy order. At $\vartheta/\pi \approx 0.80$, the energy barrier is the largest. When $\vartheta/\pi = 1.00$ the the energy barrier is zero, which is consistent with the gapless Goldstone modes of the $SU(2)$ Heisenberg model.

The analysis above implies that, if we choose $\mathbf{n} = \mathbf{b}$ as the magnetically ordered moment direction and $\mathbf{e} = \mathbf{c}$ as the arbitrary unit vector, then we can give the explicit formula in Eq. (SM-29),

$$\begin{cases} A = \Gamma - 3J \\ B_{\mathbf{q},\tau} = \frac{\Gamma(\omega^\tau - 3)}{2} \varrho^{-1} \cos \pi k \\ C_{\mathbf{q},\tau} = \frac{\Gamma\omega^\tau}{2} \varrho^2 \\ D_{\mathbf{q}} = -2J\varrho^{-1} \cos \pi k \\ E_{\mathbf{q}} = \frac{2J + \Gamma}{2} \varrho^2 \end{cases}. \quad (\text{SM-30})$$

where $\omega = \frac{1+2\sqrt{2}i}{3}$.

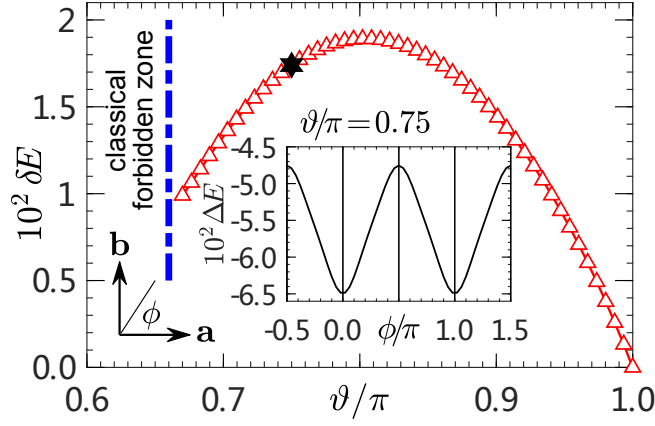


FIG. SM-5: Energy barrier δE between the stripy phases of different orientations in the BMJF model vs ϑ/π . Inset: Quantum energy correction $\Delta E(\phi)$ vs angle ϕ suited at the \mathbf{a} - \mathbf{b} plane.

two-sublattice AFM Néel order.

The AFM Néel order only has two sublattices. Without loss of generality we can assume that $\tau = +1$ for the \mathcal{A} -sublattice and $\tau = -1$ for the \mathcal{B} -sublattice. Quite directly, we can obtain

$$\begin{aligned} \mathcal{H} = & -N_s S(S+1) [-J + 2\Gamma(\zeta^y \zeta^z + \zeta^z \zeta^x + \zeta^x \zeta^y)] \\ & + \frac{S}{2} \sum_{\mathbf{q}} \begin{pmatrix} a_{\mathbf{q}} \\ b_{\mathbf{q}} \\ a_{-\mathbf{q}}^\dagger \\ b_{-\mathbf{q}}^\dagger \end{pmatrix}^\dagger \begin{pmatrix} \varepsilon_0 & \lambda_0(\mathbf{q}) & 0 & \lambda_1(\mathbf{q}) \\ \lambda_0^*(\mathbf{q}) & \varepsilon_0 & \lambda_1(-\mathbf{q}) & 0 \\ 0 & \lambda_1^*(-\mathbf{q}) & \varepsilon_0 & \lambda_0^*(-\mathbf{q}) \\ \lambda_1^*(\mathbf{q}) & 0 & \lambda_0(-\mathbf{q}) & \varepsilon_0 \end{pmatrix} \begin{pmatrix} a_{\mathbf{q}} \\ b_{\mathbf{q}} \\ a_{-\mathbf{q}}^\dagger \\ b_{-\mathbf{q}}^\dagger \end{pmatrix} \end{aligned} \quad (\text{SM-31})$$

where

$$\begin{cases} \varepsilon_0 = -J + 2\Gamma(\zeta^y \zeta^z + \zeta^z \zeta^x + \zeta^x \zeta^y) \\ \lambda_0(\mathbf{q}) = \Gamma[\mathcal{G}_{\tau=1}^{yz}(-1)e^{i\mathbf{q}\delta_x} + \mathcal{G}_{\tau=1}^{zx}(-1)e^{i\mathbf{q}\delta_y} + \mathcal{G}_{\tau=1}^{xy}(-1)e^{i\mathbf{q}\delta_z}] \\ \lambda_1(\mathbf{q}) = [-J(e^{i\mathbf{q}\delta_x} + e^{i\mathbf{q}\delta_y} - e^{i\mathbf{q}\delta_z}) + \Gamma[\mathcal{G}^{yz}(1)e^{i\mathbf{q}\delta_x} + \mathcal{G}^{zx}(1)e^{i\mathbf{q}\delta_y} + \mathcal{G}^{xy}(1)e^{i\mathbf{q}\delta_z}]] \end{cases} \quad (\text{SM-32})$$

if we choose the following crystalline axis, namely, $\mathbf{e} = \mathbf{a}$ $[11\bar{2}]$, $\mathbf{n} \times \mathbf{e} = \mathbf{b}$ $[\bar{1}10]$, and $\mathbf{n} = \mathbf{c}^*$ $[111]$, then we have

$$[\zeta_\alpha \zeta_\beta] = \frac{1}{3} \begin{pmatrix} 1 & 1 & 1 \\ 1 & 1 & 1 \\ 1 & 1 & 1 \end{pmatrix}, \quad [\mathcal{G}^{\alpha\beta}(1)] = \frac{1}{3} \begin{pmatrix} 2 & -1 & -1 \\ -1 & 2 & -1 \\ -1 & -1 & 2 \end{pmatrix}, \quad [\mathcal{G}_{\tau=1}^{\alpha\beta}(-1)] = \frac{2}{3} \begin{pmatrix} \omega^{-1} & 1 & \omega \\ 1 & \omega & \omega^{-1} \\ \omega & \omega^{-1} & 1 \end{pmatrix} \quad (\text{SM-33})$$

where $\omega = e^{2\pi i/3}$. In light of above equations we find that

$$\begin{cases} \varepsilon_0 = 2\Gamma - J \\ \lambda_0(\mathbf{q}) = -\varrho^{-1} [2(\Gamma/3 + J) \cos \pi k + (\Gamma/3 - J)(-1)^h] \\ \lambda_1(\mathbf{q}) = \frac{2\Gamma}{3} \varrho^{-1} [(-\cos \pi k + \sqrt{3} \sin \pi k) + (-1)^h] \end{cases} \quad (\text{SM-34})$$

Spin-wave dispersion ω_{qv} , energy ε , and sublattice magnetization M

In this section we mainly focus on the spin-wave results of the four-sublattice zigzag/stripy order. For the rectangular $a \times b$ magnetic unit cell ($3a_0 \times \sqrt{3}a_0$ in terms of lattice spacing a_0 ; see Fig. (1)(a) of the main

text), we define the wave vector \mathbf{q} in units of (h, k) as $\mathbf{q} = (\frac{2\pi}{a}h, \frac{2\pi}{b}k)$. The four spin-wave dispersion branches ω_{qv} ($v = 1-4$) for the zigzag order ($\vartheta/\pi = 0.25$) and stripy order ($\vartheta/\pi = 0.75$) are shown in Fig. (SM-6). It can be found that the former is gapped while the latter is gapless. The Goldstone modes of the latter come from the emergent continuous $U(1)$ symmetry. As demonstrated

in Fig. (SM-5), those macroscopic degeneracy would be lifted via an order-by-disorder mechanism, selecting only two of them that break lattice rotational symmetry.

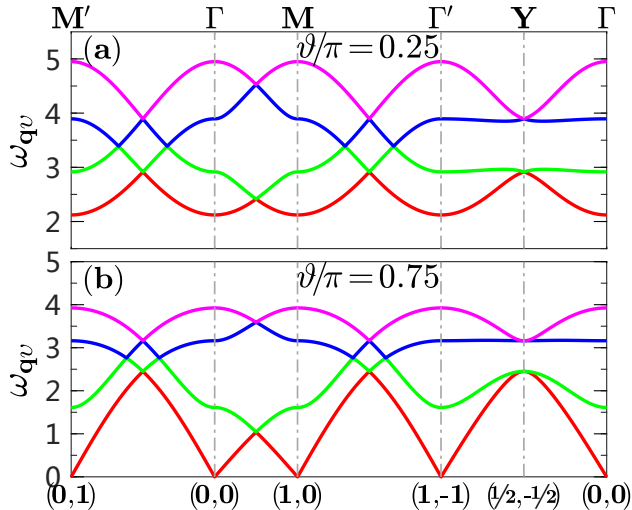


FIG. SM-6: (a) and (b) show the magnon spectra in the zigzag phase ($\vartheta/\pi = 0.25$) and stripy phase ($\vartheta/\pi = 0.75$), respectively. The path along the symmetry directions in the momentum space is depicted in Fig. (1)(b) of the main text.

Next, it is straightforward to calculate the spin-wave energy ε and sublattice magnetization M . The full results are shown in Fig. SM-7. The black solid lines is the classical energy for all the phases. The transitions between each of the two are of first order because of the kinks in the energy curve. In the zigzag phase, the energy correction ΔE (when compared to the classical energy) is the largest at $\vartheta/\pi = 0.50$, which is about 0.080. This means that there is a large quantum fluctuation for the HCGA. In contrast, in the intermediate region, the energy correction for the Néel phase is very small, indicating that the Néel order is unlikely the true ground state at the quantum level. We emphasize here that this phenomenon is directly related to the QSL phase by large-scale DMRG calculation.

For either zigzag or stripy phase, the four different branches of sublattice magnetization, corresponding to the four flavors of bosons, are discrepant, implying a sublattice symmetry breaking. For simplicity, we only consider the lowest branch in their corresponding classical regions, see Fig. SM-7(b). The maximal positions of the magnetization $\langle M \rangle$ locate at $\vartheta/\pi \approx 0.20$ for the zigzag phase and $\vartheta/\pi \approx 0.85$ for the stripy phase. These positions are very close to the quantum case. The most important result is that, the magnetization $\langle M \rangle$ of the zigzag phase totally vanishes at $\vartheta/\pi = 0.50$. This suggests that the ground state of HCGA is likely a QSL in the quantum situation.

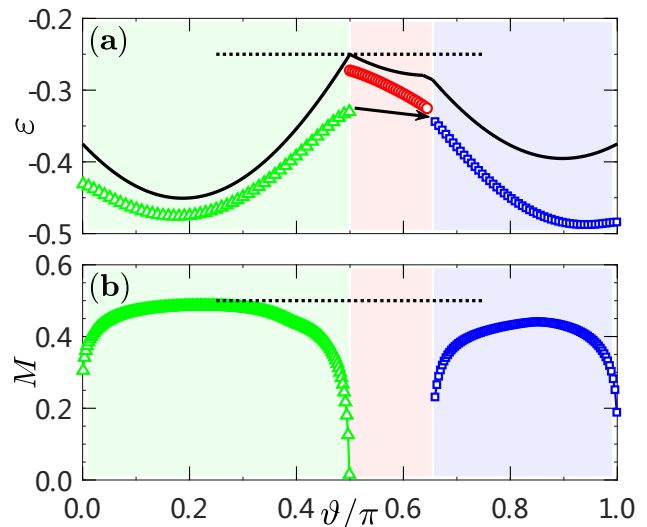


FIG. SM-7: (a) The LSWT energy for zigzag order (green), Néel order (red), and stripy order (blue). The black line is the classical energy (S is set to be 1/2) illustrated in the main text. The black arrow indicates a small energy difference between the transition points and the energy fluctuation promises to be tiny in the quantum system (see Fig. 3(a) of the main text). (b) The lowest branch of the sublattice magnetization for the zigzag order and stripy order.

QUANTUM GROUND STATE OF THE BMJΓ MODEL: ENERGY, ENTROPY, AND STRUCTURE FACTORS

Energy and energy gap of the HCGA

In this section we want to obtain the ground-state energy e_g and energy gap Δ of HCGA ($\vartheta/\pi = 0.5$). To begin with, we plot the first three energy levels around $\vartheta/\pi = 0.5$ in the XC cluster of 12×6 , see Fig. SM-8(a). It can be seen clearly that, when away from the transition point, the energy difference between the two lowest levels in the zigzag phase are exponentially small, indicating that the ground state is two-fold degenerate in the thermodynamic limit. With the increasing of ϑ , the quasi-degeneracy is lifted gradually, which becomes visible near the transition point. Such a level splitting is still preserved even in the QSL phase, resulting in a unique ground state at finite size. In fact, exact diagonalization of the HCGA under hexagonal clusters of $N = 24$ and 32 sites (see Fig. SM-12) also finds a unique ground state, followed by a two-fold degenerate first excited state.

Hereafter, we will focus on HCGA. Instead of considering only the case of $L_x/L_y = 2$, we adopt a series of acceptable ratios ranging from 1.5 to 4.0. Firstly, we fit the total energy E_g v.s. N , as shown in Fig. SM-8(b). The raw fitting gives us that $E_g = -0.352(4)N - 0.06(12)$. Secondly, for each circumference $n = 4, 6$, and 8, we fit the energy per-site $e_g = E_g/N$ v.s. $1/N$, see Fig. SM-8(c).

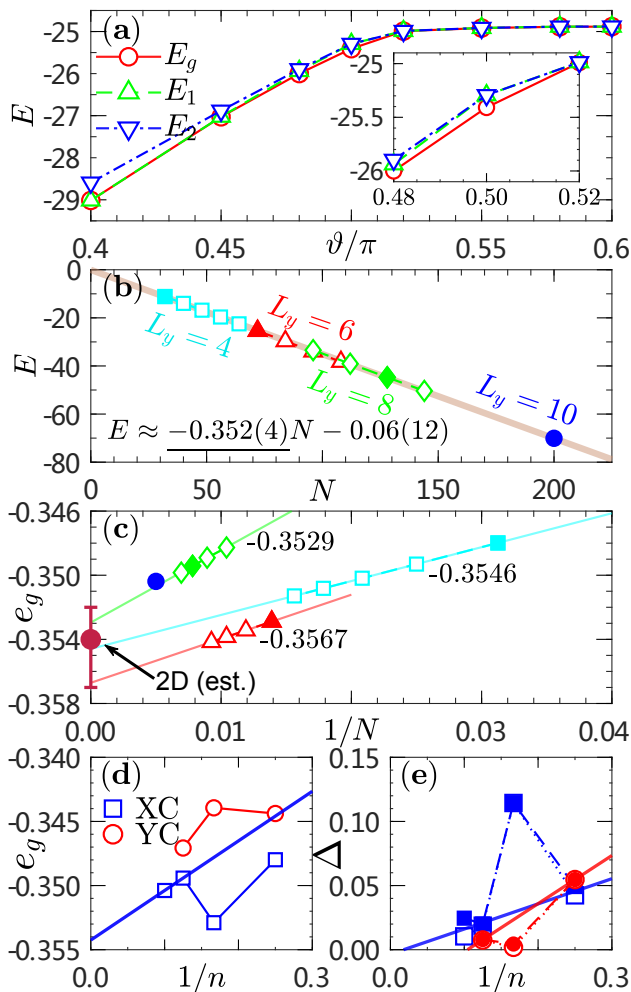


FIG. SM-8: (a) The first three energy levels of the BMJT model under XC cluster of 12×6 . The inset zooms in the energy levels near HCTA. (b) The overall fitting of the total energy E_g v.s. N . (c) Linearly fitting of the energy e_g v.s. $1/N$ for each XC_n cluster. (d) Ground-state energy e_g for HCTA on XC (blue) and YC (red) clusters. The width n of the clusters ranges from 4 to 10. (e) Energy gaps Δ_1 (open symbols) and Δ_2 (filled symbols) for the corresponding clusters. The thick solid lines indicate the overall trends of the curves.

It can be found that e_g is almost linearly decreasing with $1/N$, and the estimated energies at TDL fall in the band of -0.357 and -0.352 . However, when crossing from 4 to 8, the energy does not have a monotonic behavior. Such a nonmonotonic energy dependence of the size can be further checked by focusing on the energy at $L_x/L_y = 2$ for both XC and YC cylinders, see Fig. SM-8(d). Because of the abnormal behavior at $L_y = 6$, for the XC cluster the energy is smaller than the “expected” value, while for the YC case it is somehow reversed. We recall that the gap for vison excitations in the Kitaev model shows a three-period structure, as pointed out by Kitaev[5]. We thus speculate that the energy spectra of HCTA may also

own a similar periodicity. The unusual behavior of the ground-state energy has an awful impact on the energy gaps shown in Fig. SM-8(e), making an accurate extrapolation to the thermodynamic limit intractable. Since the overall downward trend in the gaps with the increasing of the system size, we can still identify that the gaps, $\Delta = 0.00(1)$, closes eventually. Moreover, as shown in Fig. 3(b) of the main text, the excitation spectrum of HCTA is extremely dense, and this is a strong evidence for the gapless systems.

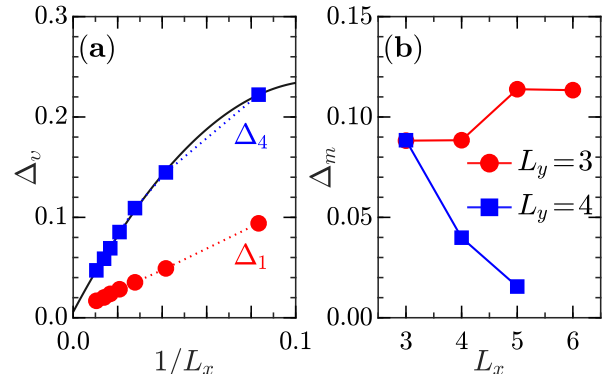


FIG. SM-9: (a) Energy gap $\Delta_v = E_v - E_0$ for a two-leg honeycomb ladder under PBC. The black line is the extrapolation of Δ_4 to infinite-size system. (b) The minimal energy gap Δ_m for the three-leg (red circle) and four-leg (blue square) tori.

Gaplessness and entanglement entropy scaling

In this subsection we go beyond the XC clusters, and study the energy gap of the pure Γ model ranging from 1D chain to two-leg honeycomb ladder, and also towards a series of $2 \times L_x \times L_y$ tori of $L_y = 3$ or 4. The geometry of the latter is shown in the inset of Fig. 4 in the main text.

- To begin with, for the 1D isotropic Γ chain, its ground state is found to be a gapless Luttinger liquid with emergent $SU(2)$ symmetry[6].
- Furthermore, we consider a two-leg honeycomb ladder which is a rung-alternating coupling of two isotropic Γ chain. It is a stripe of a honeycomb lattice along its zigzag edges and only contains $L_x/2$ Z bonds. We find that there is a unique ground state with energy E_0 under PBC, followed by a triplet excited state with energy E_1 . There seems to be a continuous spectrum afterwards and the lowest branch has a energy of E_4 . Figure SM-9(a) shows the energy gap of $\Delta_1 = E_1 - E_0$ and $\Delta_4 = E_4 - E_0$, which go down as L_x increased. After an extrapolation of Δ_4 we find that $\Delta_4 < 0.004$, which seems to close for long enough ladder.

- Moreover, we study the energy gaps for three- and four-leg tori. Here, PBCs are imposed on both directions so as to remove the possible edge excitations. For $L_y = 3$, we perform the calculation on four different tori with $L_x = 3, 4, 5$, and 6, and find that the gap is around ~ 0.11 . However, for $L_y = 4$, the gap goes down quickly from 0.09 when $L_x = 3$ to 0.015 when $L_x = 5$, see Fig. SM-9(b). We thus infer that the gap for $L_y = 4$ most probably vanishes as $L_x \rightarrow \infty$.

The results on different clusters are summarized in the table below. We find that the energy gap has a strong cluster dependence, and could vanishes at several cases. We note that this is not the typical character of a gapped system whose gap is usual very stable. In this regard, it is another evidence for the gaplessness of HCTA.

TABLE SM-1: Energy gap of the pure Γ model under a 1D chain, two-leg honeycomb ladder, and also $2 \times L_x \times L_y$ tori of $L_y = 3$ or 4.

Cases	Energy gap	Gapped/Gapless
1D isotropic Γ chain	0	gapless
two-leg honeycomb Γ ladder	< 0.004	gapless
$2 \times L_x \times 3$ torus	~ 0.11	gapped
$2 \times L_x \times 4$ torus	< 0.001	gapless

To further shed light on the critical behavior of HCTA, we calculate the von Neumann entanglement entropy \mathcal{S} . Suppose that the entire system is divided into two parts, say s and e , then the entropy is defined as $\mathcal{S} = -\text{Tr}(\rho_s \ln \rho_s)$ where the reduced density matrix $\rho_s = \text{Tr}_e |\psi\rangle\langle\psi|$ is obtained by tracing out the degrees of freedom of e . To access large cluster with $L_x \gg L_y$, we adopt the cylinder geometries which are open (periodic) in L_x (L_y)-direction. For such a (1+1)-D critical system, it is known that $\mathcal{S}(x) = \frac{c}{6} \ln \left(\frac{2L_x}{\pi} \sin \frac{\pi x}{L_x} \right) + c'$ where c is the central charge[7].

For cylinder of $L_y = 3$, it is gapped and the entropy does not goes with L_x (not shown). In contrast, cylinder of $L_y = 4$ is gapless and there is a perfect entanglement entropy scaling as shown in Fig. 4 of the main text. The central charge $c \approx 1.09$, which is very close to 1. In addition, We also calculate the entanglement entropy on a series of similar cylinders of $2 \times (2L) \times L$ with total site $N = 4L^2$. Here, $L = 3, 4, 5$, and 6. As shown in Fig. SM-10, we fit the entanglement entropy by $\mathcal{S} = kL \ln L + b$ and find that the goodness-of-fit is acceptable. The fact that the entanglement entropy grows with L but has a logarithmic correlation, i.e, $\mathcal{S} = \mathcal{O}(L^{D-1} \ln L)$ with $D = 2$, is fairly consistent with the 2D critical system[7].

Before we end this subsection, we want to address that the significant difference between $L_y = 3$ and 4 suggests an unusual way from multi-leg ladder towards 2D limit. Besides, it may imply that the ground state is likely to own spinon fermi surface, as discussed in the case of

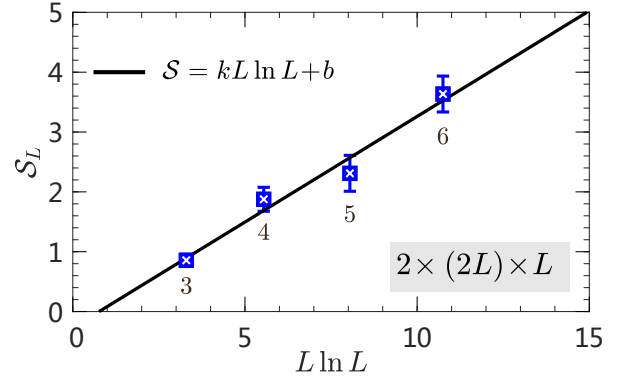


FIG. SM-10: The entanglement entropy for different cylinders of $2 \times (2L) \times L$ with $L = 3, 4, 5$, and 6. The error bar becomes large as L increased. The black solid line is the fitting by $\mathcal{S} = kL \ln L + b$ with $k \approx 0.35$.

Kitaev model under magnetic field[8, 9]. Figure SM-11 shows the quantized momenta along the circumference of the three-leg (left) and four-leg (right) cylinders. In view of the different central charges of the two cases, we speculate the gapless excitations meet one of the red lines in Fig. SM-11(b) rather than the green lines in Fig. SM-11(a). However, since there is no translational symmetry along the L_x -direction (OBC), we cannot determine the precise momenta of the gapless excitations.

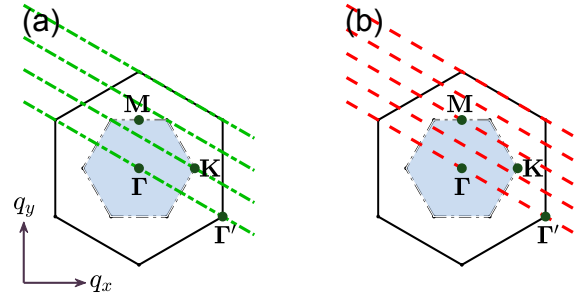


FIG. SM-11: The quantized momenta along the circumferences of the cylinders of $L_y = 3$ (left) and $L_y = 4$ (right).

Lattice nematic order and plaquette correlation

In most cases of our DMRG calculation, the cylinder geometries are preferred since it can be used to access a very large cluster with a few hundred sites. However, those geometries break the lattice rotational symmetry and suffer from a strong finite-size effect. Therefore, in some special situations we turn to the hexagonal clusters. Due to the limitation of the storage memory, we usually use the hexagonal clusters of $N = 24$ and 32, see Fig. SM-12. Within the hexagonal clusters, we mainly undertake two things. One is the lattice nematic order while the other is the flux density and plaquette correlation.

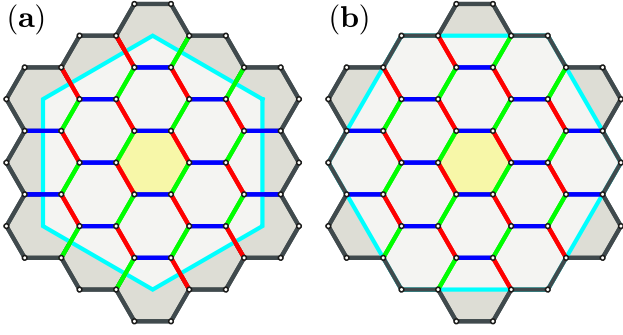


FIG. SM-12: The lighted region with a cyan frame marks a hexagonal cluster of (a) $N = 24$ and (b) $N = 32$.

Figure SM-13(a) and (b) show the landscapes of the bond energy for $\vartheta/\pi = 0.50$ and $\vartheta/\pi = 0.60$. It is observed that the energy is uniformly distributed along each γ -bond. Because of the bond-modulated η_γ -factor, there is naturally a bond energy difference between the \mathbf{X}/\mathbf{Y} ($\eta_\gamma = -1$) bond and the \mathbf{Z} ($\eta_\gamma = 1$) bond. The bond energy for $\vartheta/\pi = 0.50$ is uniform while there is a difference otherwise, i.e., nematicity. It should be emphasized that the bond energy of \mathbf{X} and \mathbf{Y} are always equal, and the nematicity between \mathbf{X}/\mathbf{Y} and \mathbf{Z} bonds comes from the η_γ -factor but not the lattice rotational symmetry breaking. In Fig. SM-13(c) we show the lattice nematic order parameter $\mathcal{N} = E_{x/y} - E_z$ under hexagonal clusters of $N = 24$ and 32 . When away from HCGA ($\vartheta/\pi = 0.50$), \mathcal{N} is very robust except for two *accidental* points at $\vartheta/\pi \approx 0.25$ and 0.75 . Interestingly, this two points are in coincidence with the extreme points of magnetic orders shown in Fig. 5(a) of the main text.

In the Kitaev honeycomb model, the low-energy physics of the Kitaev spin liquid is described by Majorana fermions with Dirac nodes, coupled to an emergent \mathbb{Z}_2 gauge field[5]. The hexagonal plaquette operator $W_p = 2^6 S_1^x S_2^y S_3^z S_4^x S_5^y S_6^z$ commutates with the model and $W_p = \pm 1$. A particle that moves in a loop around the plaquette acquires a phase ± 1 similar to an Aharonov-Bohm like flux of either 0 or π . For $W_p = +1$ the plaquette is called flux-free and for $W_p = -1$ it has a flux. The former is the ground state while the latter is the excited state with a vison excitation[5].

For the HCGA as well as the general BMJF model, $[\mathcal{H}, W_p] \neq 0$, so W_p is no longer a conserved quantity. However, the flux density $\langle \overline{W}_p \rangle = \sum_p \langle W_p \rangle / N_p$ where $N_p = N/2$ is the number of hexagonal plaquette can be tremendously useful and informative to distinguish different phases. As shown in Fig. SM-14(b), $\langle \overline{W}_p \rangle = -0.25(2)$ in the TDL.

Moreover, we calculate the plaquette-plaquette correlation $\langle W_p W_q \rangle$, and define the static visonic structure

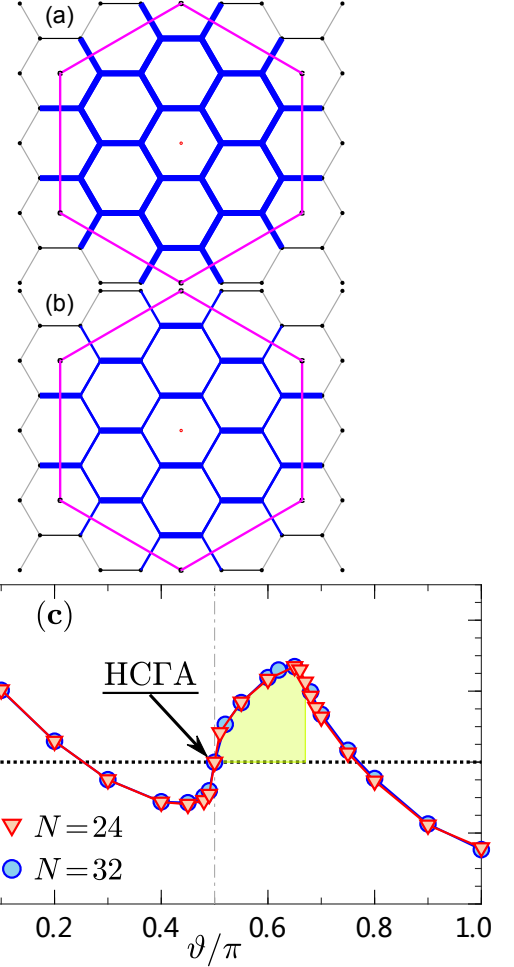


FIG. SM-13: Landscapes of the bond energy at (a) $\vartheta/\pi = 0.50$ and (b) $\vartheta/\pi = 0.60$ under the hexagonal cluster of $N = 24$. The width of the bonds is proportional to the energy strength.

factor[10],

$$\mathcal{W}_{N_p}(\mathbf{Q}) = \frac{1}{N_p} \sum_{pq} \langle W_p W_q \rangle e^{i\mathbf{Q} \cdot (\mathbf{R}_p - \mathbf{R}_q)}, \quad (\text{SM-35})$$

where \mathbf{R}_p is the central position of each plaquette. We find that there is a dominating peak in the Γ point and also a subleading peak at \mathbf{K} point of the Brillouin zone. This fact implies that there is no translational symmetry breaking in the honeycomb lattice but with perceptible plaquette correlation. We thus define the *pseudo* order parameter (POP) as $\mathcal{P}_{N_p} = \sqrt{\mathcal{W}_{N_p}(\mathbf{Q})/N_p}$. The results on the hexagonal clusters of $N = 24$ and 32 are shown in Fig. SM-14(a). Due to the dominating contribution from the trivial identity $\langle (W_p)^2 \rangle = 1$ [18], \mathcal{P}_{N_p} has a considerable finite-size value, which is approximately $1/\sqrt{N_p}$, see the horizontal lines in Fig. SM-14. Therefore, the bared POP is formally defined as

$$\overline{\mathcal{P}}_{N_p} = \sqrt{\frac{\mathcal{W}_{N_p}(\mathbf{Q})}{N_p}} - \frac{1}{\sqrt{N_p}}. \quad (\text{SM-36})$$

The result of the bared POP is shown in Fig. 6 of the main text. It can be found that there is a plaquette correlation near HCGA. Besides, there is a negative flux density $\langle \bar{W}_p \rangle = -0.25(2)$ for HCGA.

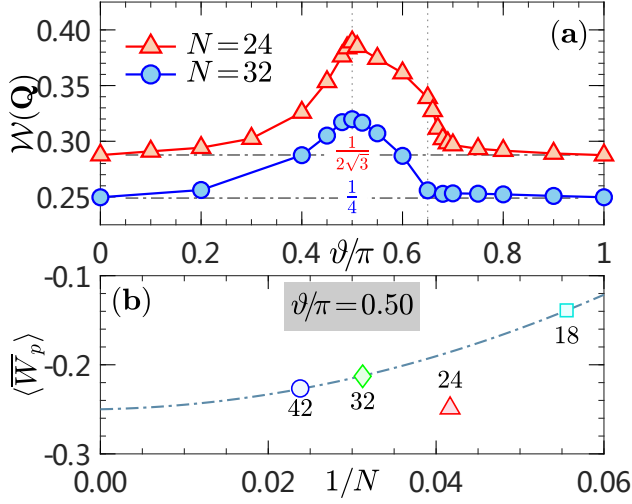


FIG. SM-14: (a) SVSF $W(\mathbf{K})$ on hexagonal clusters of $N = 24$ and 32. The horizontal lines of $1/(2\sqrt{3})$ and $1/4$ are approximately the lower limits at the corresponding sizes. (b) Extrapolated flux density $\langle \bar{W}_p \rangle$ for HCGA.

Phase diagram and magnetic structure factor

As shown in Fig. SM-7, the mixed phase (taking the AFM Néel order as an example) is not favored by quantum fluctuations. Indeed, in the quantum case, the SMSF in this region is almost featureless and the existing peaks are very weak at the finite clusters. Extrapolations of the maximal values of the SMSF (see Fig. (4)(b)-(c) of the main text) shows that this is a QSL phase, as confirmed by scanning a long cylinder shown in the last Section. Notably, our results only support a single intermediate phase other than two as discussed in the classical phase diagram. We refer to the argument for a similar anisotropic model for the QSL candidate YbMgGaO_4 [11]. Whereas a so-called multi- \mathbf{Q} phase exists between two magnetically ordered phases[12] in the classical level, extensive numerical calculations do not detect its trail in the quantum case, but instead suggest a direct first-order transition[13, 14].

The entanglement entropy \mathcal{S} is a sensitive probe for quantum phase transition, and it is frequently used to characterize different phases. The result of the entropy on hexagonal clusters of $N = 24$ and 32 and on XC clusters of 12×6 , 16×8 , and 20×10 is shown in Fig. SM-15(a) and (b), respectively. In both cases we can declare two most pronounced phenomena. One is that the entropy has a sudden drop at $\vartheta_l/\pi \simeq 0.50$ and $\vartheta_r/\pi \approx 0.66$, indicating that both of the transitions are of first order. The

other is that the entropy in the gapped zigzag and stripy phases are lower than that in the intermediate phase. Besides, with the increasing of the total sites, the entropy in the intermediate phase increases. This agrees with our conclusion that the intermediate phase is gapless.

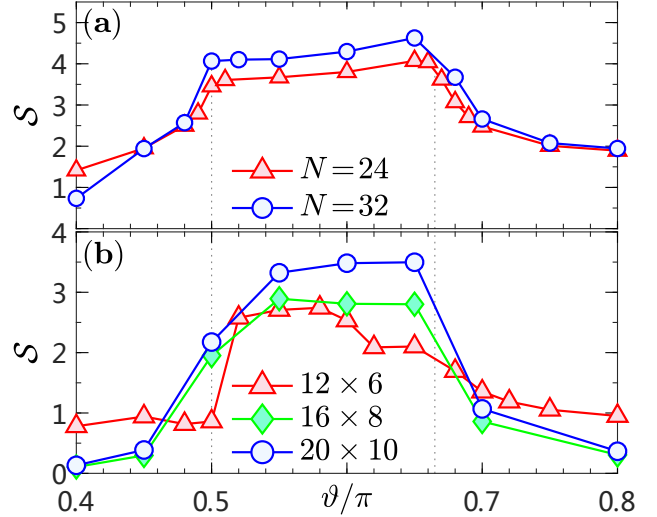


FIG. SM-15: The von Neumann entropy \mathcal{S} for ϑ/π ranging from 0.4 to 0.8. (a) Hexagonal clusters with the a total sites $N = 24$ (red triangle) and 32 (blue circle). (b) XC clusters with the circumference n be 6 (red triangle), 8 (green diamond), and 10 (blue circle).

The entire phase diagram is shown in Fig. SM-16, which includes a zigzag order and a stripy order, and also a QSL. The ground state of HCGA locates at the transition point between the zigzag order and the QSL. The selected contour plots of the SMSF for the three phases are shown in Fig. SM-16(a)-(c). While the zigzag and stripy phases peak at \mathbf{M} and/or \mathbf{M}' points, the magnetic order at $\vartheta/\pi = 0.5$ is tiny, and a subleading peak locating at \mathbf{X} point in the Brillouin zone appears. This peak could be enhanced by negative third-NN interaction (see below).

Role of third-NN Interaction

Recent *ab initio* calculations on $\alpha\text{-RuCl}_3$ have highlighted the role played by the third-NN Heisenberg interaction $J_3 \sum_{\langle\langle\langle i,j \rangle\rangle\rangle} \mathbf{S}_i \cdot \mathbf{S}_j$. It is shown that even a tiny antiferromagnetic J_3 can enhance the zigzag magnetic order[15]. This physical virtue has already been examined in other theoretical models where competing interactions could lift the degeneracy of the pure J_3 model and give rise to the zigzag order. To verify such conclusions we study the Γ - J_3 model to explore the effect of the J_3 term. We find that in the phase diagram the HCGA is indeed adjacent to the zigzag phase but separated by a transition.

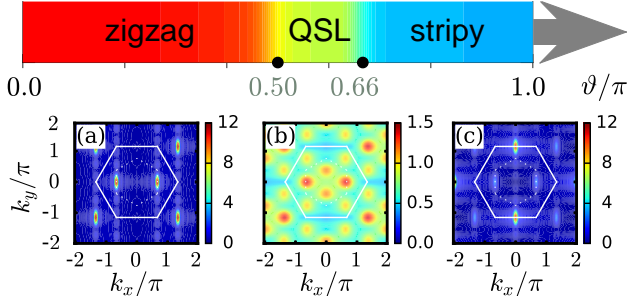


FIG. SM-16: Quantum phase diagram of the BMJF model on a honeycomb lattice. The shade of color is a reminiscence of the corresponding magnetic order. Typical contour plots of the overall SMSF for (a) zigzag phase ($\vartheta/\pi = 0.25$), (b) QSL phase ($\vartheta/\pi = 0.50$), and (c) stripy phase ($\vartheta/\pi = 0.75$) are shown for XC clusters of 12×6 .

Fig. SM-17 shows the evolution of the magnetic orders versus J_3 in a rather wide region. It could be found that the ferromagnetic and antiferromagnetic J_3 model tend to select the FM phase and zigzag phase, respectively, as the ground state with the perturbation of antiferromagnetic Γ term. Between the two, the maximum of $M_N(\mathbf{Q})$ appears at \mathbf{X} point of the Brillouin zone (see Fig. 1 of the main text). At $J_3 = 0$, $M_N(\mathbf{Q})$ at \mathbf{M} becomes comparable to that at \mathbf{X} . However, as can be seen from the inset which shows the first derivative of $M_N(\mathbf{M})$ versus J_3 , the peak locates at a tiny but nonzero $J_{3,t} \approx 0.075$. This provides further evidence that the ground state of the HCTA, in which J_3 is zero, is not the zigzag order.

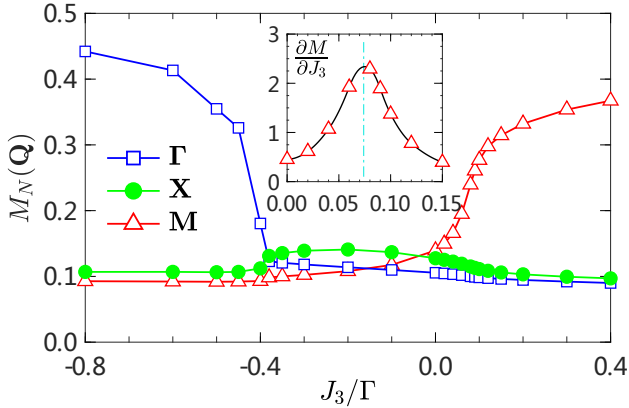


FIG. SM-17: Order parameters $M_N(\mathbf{Q})$ for the FM order (blue square), X-order (green circle), and zigzag order (red triangle) with $\mathbf{Q} = \Gamma, \mathbf{X}$, and \mathbf{M} , respectively. The circumference n of the cluster is fixed to be 6. Inset: The first derivative of $M_N(\mathbf{M})$ versus J_3 .

IDEAS ON THE LONG CYLINDER

In this section we resort to a complementary technique proposed by Zhu *et al.*[14, 16, 17] to provide further evi-

dences for the QSL phase in Eq. (1) of the main text. We adopt a long but finite cylinder of 36×6 , which could be regarded as a triplet assembly of the conventional geometry. We now present the details on how to scan the long cylinder within the DMRG method[16]. This technique is born to detect the intermediate disordered phase sandwiched between two magnetically ordered phases and has been successfully applied to several different models. To carry out the calculation, there are two apparent issues that should be settled when compared to the traditional DMRG construction. On one hand, proper pinning fields which are compatible with the underlying magnetic orders should be applied to the edge spins. To accelerate the convergence as well as to induce meaningful pinning orders, we shall apply pinning fields of order $\mathcal{O}(1)$ and fix the directions of the three components as they appear in their classical counterparts. On the other hand, the driven interactions should vary with the position, from the left to the right. In our current model, we fix the interactions at the leftmost and rightmost boundaries, say $\vartheta_{\min}/\pi = 49/120$ and $\vartheta_{\max}/\pi = 91/120$. The interactions inside will vary according to a presupposed protocol, which could be merely the linear rule. Because we only consider the nearest-neighbor interactions J and Γ along the three bonds, we can distinguish the zigzag (\mathbf{X} and \mathbf{Y}) bonds to the horizontal (\mathbf{Z}) bond so as to make the variation of ϑ be more smooth. The variation of ϑ with position is illustrated in Fig. SM-18, and for each ϑ -index shown in the bottom, we have the current value $\vartheta_x = \vartheta_{\min} + x \cdot \delta\vartheta$ where $\delta\vartheta = (\vartheta_{\max} - \vartheta_{\min})/[2(L_x - 1)] = 0.005\pi$ in our case. This is to say that there is a 0.01π increment for the two successive columns ranging from 0 to $L_x - 1$.

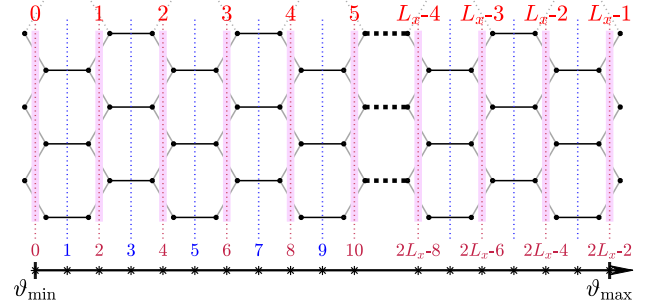


FIG. SM-18: Illustration on the variation of the ϑ with position. The series ranging from 0 to $L_x - 1$ shown in the top denotes the column index. The other series ranging from $(x =) 0$ to $2(L_x - 1)$ shown in the bottom denotes the ϑ -index. The value of ϑ in the vertical dotted line is $\vartheta_x = \vartheta_{\min} + x \cdot \delta\vartheta$ where $\delta\vartheta = (\vartheta_{\max} - \vartheta_{\min})/[2(L_x - 1)]$.

For a long XC cylinder of 36×6 , we present the visual display of the spin configuration in Fig. SM-19. Here, the arrows represent the classical $O(3)$ spin. The length indicates local measurement of $\langle S_{\text{tot}} \rangle =$

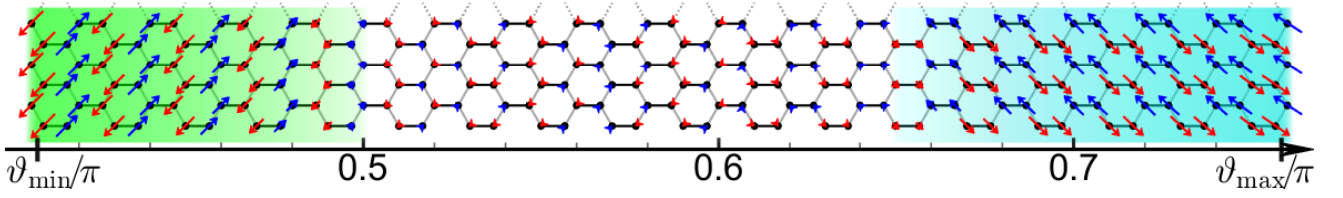


FIG. SM-19: For a long XC cylinder of $L_x \times L_y = 36 \times 6$, we vary ϑ/π with position, from $\vartheta_{\min}/\pi = 49/120$ on the left edge to $\vartheta_{\max}/\pi = 91/120$ on the right edge. We also apply pinning magnetic fields along all the three spin directions on the left (right) edge to favor the classical zigzag (stripy) order. An intermediate phase without the shadow is revealed to sandwich between the two.

$\sqrt{\langle S_x \rangle^2 + \langle S_y \rangle^2 + \langle S_z \rangle^2}$ and the direction is the ϕ -angle given by Eq. (SM-1). We find that there is a zigzag magnetic order in the left and a stripy magnetic order in the right. In the intermediate region, the orientation of spins are amorphous and the magnetic order (indicated by the length of the spins) is rather small, indicating of a plausible disordered phase.

Fig. SM-20 shows the local ordered moment $\langle S_{\text{tot}} \rangle$, which shows an artificial upwarping at the boundaries due to the pinning fields. The x and y components have an almost equal magnitude all the way while the z component in the stripy phase is negligible. The total moment in the middle is rather weak and we use a threshold value of $\langle S_{\text{tot}} \rangle \approx 0.10$ as the upper limit for the QSL phase[14, 16, 17]. The rough phase boundaries ($0.50 \leq \vartheta/\pi \leq 0.65$) are fairly consistent with those obtained in preceding DMRG calculations. It should be noted that although the pinning order at $\vartheta/\pi = 0.5$ is not small enough, we would expect a rapid decay once we can access larger clusters. It is in this sense that we confirm the robustness of the QSL phase in the quantum phase diagram (see Fig. SM-16).

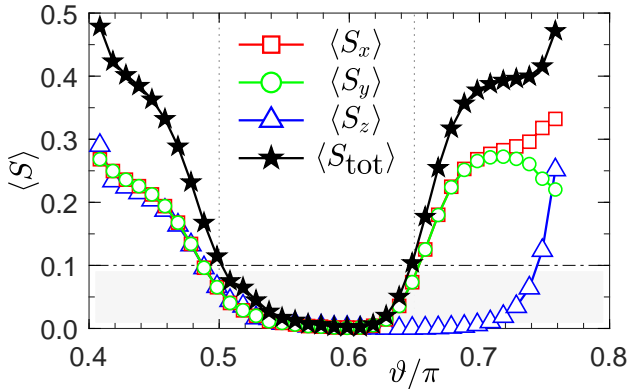


FIG. SM-20: Local moment $\langle S_{\text{tot}} \rangle = \sqrt{\langle S_x \rangle^2 + \langle S_y \rangle^2 + \langle S_z \rangle^2}$ vs ϑ for XC cluster of 36×6 . The dot dash horizontal line marks the threshold value, while the dotted vertical lines denote the possible phase boundaries.

* zhaojz@lzu.edu.cn

† xiaoqunwang@sjtu.edu.cn

- [1] I. Rousochatzakis and N. B. Perkins, Phys. Rev. Lett. **118**, 147204 (2017).
- [2] J. G. Rau, E. K.-H. Lee, and H.-Y. Kee, Phys. Rev. Lett. **112**, 077204 (2014).
- [3] L. Janssen and M. Vojta, J. Phys.: Condens. Matter **31**, 423002 (2019).
- [4] S. K. Choi, R. Coldea, A. N. Kolmogorov, T. Lancaster, I. I. Mazin, S. J. Blundell, P. G. Radaelli, Yogesh Singh, P. Gegenwart, K. R. Choi, S.-W. Cheong, P. J. Baker, C. Stock, and J. Taylor, Phys. Rev. Lett. **108**, 127204 (2012).
- [5] A. Kitaev, Ann. Phys. **321**, 2 (2006).
- [6] W. Yang, A. Nocera, T. Tummuru, H.-Y. Kee, and I. Affleck, Phys. Rev. Lett. **124**, 147205 (2020).
- [7] J. Eisert, M. Cramer, and M. B. Plenio, Rev. Mod. Phys. **82**, 277 (2010).
- [8] H.-C. Jiang, C.-Y. Wang, B. Huang, and Y.-M. Lu, arXiv:1809.08247 (2018).
- [9] N. D. Patel and N. Trivedi, Proc. Natl. Acad. Sci. USA **116**, 12199 (2019).
- [10] P. Saha, Z. Fan, D. Zhang, and G.-W. Chern, Phys. Rev. Lett. **122**, 257204 (2019).
- [11] Y. Li, G. Chen, W. Tong, L. Pi, J. Liu, Z. Yang, X. Wang, and Q. Zhang, Phys. Rev. Lett. **115**, 167203 (2015).
- [12] C. Liu, R. Yu, and X. Wang, Phys. Rev. B **94**, 174424 (2016).
- [13] Q. Luo, S. Hu, B. Xi, J. Zhao, and X. Wang, Phys. Rev. B **95**, 165110 (2017).
- [14] Z. Zhu, P. A. Maksimov, S. R. White, and A. L. Chernyshev, Phys. Rev. Lett. **119**, 157201 (2017).
- [15] A. Catuneanu, Y. Yamaji, G. Wachtel, Y.-B. Kim, and H.-Y. Kee, npj Quantum Materials **3**, 23 (2018).
- [16] Z. Zhu, D. A. Huse, and S. R. White, Phys. Rev. Lett. **111**, 257201 (2013).
- [17] Z. Zhu and S. R. White, Phys. Rev. B **92**, 041105(R) (2015).
- [18] Since $\langle (S^x)^2 \rangle = \langle (S^y)^2 \rangle = \langle (S^z)^2 \rangle = 1/4$, we can get $\langle (W_p)^2 \rangle = 2^{12} (\langle (S_\alpha^x)^2 \rangle)^6 = 2^{12} \cdot (1/4^6) = 1$.